CHAPTER 9

FUEL CELLS AND THEIR APPLICATIONS IN ENERGY SYSTEMS

Jih-Sheng Lai and Michael W. Ellis

9.1 INTRODUCTION

Fuel cells are most commonly applied in standalone power generation systems and vehicle energy sources because of their unique features of high efficiency, wide size range, modularity, and compatibility with cogeneration. The development of a complete fuel cell energy system requires a basic understanding of the fuel cell and supporting hardware, as well as the associated power electronics for different applications [1]. A fuel cell system produces electricity by electrochemically oxidizing a fuel source, which may consist of hydrogen or a simple hydrocarbon. The direct chemical-to-electrical conversion process can provide high energy conversion efficiency across a wide range of sizes and part-load conditions. Fuel cell systems can also be installed close to electrical loads, enabling the thermal energy provided as a by-product of the reaction to be used for cogeneration applications, making the combined efficiency even more attractive. Furthermore, fuel cells operate silently and are a dispatchable distributed generating technology. Finally, fuel cell systems typically emit extremely low levels of regulated air pollutants and provide reduced carbon dioxide emissions due to improved efficiency and near-zero carbon fuel sources.

Over the past two decades, considerable progress has been made in the development of fuel cell technology, and today, system cost and durability are the major challenges to bringing fuel cell technology to the stationary power market. In the transportation application, where hydrogen is the fuel of choice, fuel cell systems face the additional challenges of hydrogen distribution and storage. Currently, research and development continue to address these challenges [2], and the recent debut of commercially available fuel cell electric vehicles indicates growing interest

Power Electronics in Renewable Energy Systems and Smart Grid: Technology and Applications, First Edition. Edited by Bimal K. Bose.

Published 2019 by John Wiley & Sons, Inc.

from the automotive industry [3, 4]. This interest in fuel cell vehicles is motivated largely by their extended driving range and shorter refueling time relative to battery electric vehicles.

Fuel cell systems are similar to other systems for energy storage or generating devices, such as batteries and photovoltaic (PV) cells, in the sense that they can generally be described as a voltage source with an internal impedance. However, the battery internal impedance is passive, but the fuel cell internal impedance is a controlled variable that is a function of its operating conditions including reactant concentration, temperature, and humidity levels. Similarly, the PV cell is a passive device with an output primarily controlled by the solar irradiance, not by the balance-of=plant (BOP) operation. Thus, the fuel cell distinguishes itself in that it is a controllable source that produces power when needed as long as fuels are available, making it a promising candidate for portable power, transportation, uninterruptible power supply (UPS), and distributed generation applications.

Proper application of fuel cell technology requires an understanding of fuel cell system architecture, system components, steady-state and dynamic behavior, and system interaction with the load. Furthermore, the electrical connection of fuel cells has regulatory requirements, including grounding requirements that are unique compared with those of other energy generation and storage devices. The design of power electronics circuits and controls for fuel cell systems must address the overall operation of the fuel cell system while complying with the unique electrical demands associated with the particular application. This chapter provides an overview of the fuel cell system including the basic principles of fuel cell operation, the different types of fuel cells, basic fuel cell system architecture, and detailed electrical characteristics and associated power electronics. Application issues are also introduced for both transportation and stationary applications.

As illustrated in Figure 9.1, a fuel cell system typically consists of six subsystems including an air supply, fuel processing, thermal management, water management, power management, and the fuel cell stack. The *air supply system* filters the air and pressurizes, preheats, and humidifies the air as needed by the particular application. The nature of the *fuel processing system* depends on the type of application. Transportation and portable power applications typically utilize simple fuels (hydrogen or methanol) supplied directly from a storage tank, and thus the fuel supply system simply controls the flow of the fuel to the fuel cell stack. For stationary applications, however, the fuel may be a hydrocarbon such as natural gas, diesel, or biogas, and thus may require conversion to hydrogen before it is supplied to the fuel cell stack. This conversion process typically begins with a sulfur removal process that is then followed by a reforming step, which uses a catalyzed reaction at high temperature to transform the hydrocarbon to a mixture of hydrogen, carbon dioxide, and carbon monoxide. In the case of low-temperature fuel cells this initial reforming step is followed by additional steps to reduce the carbon monoxide concentration to very low levels (<50 ppm) to avoid poisoning the fuel cell catalysts. In higher-temperature fuel cells (>500 °C), carbon monoxide removal is unnecessary, and in fact, the fuel cell stack may be able to

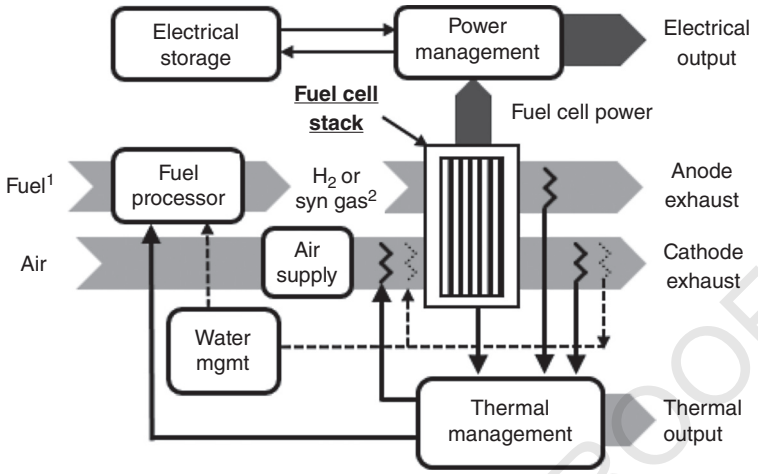

[1]Fuel consists of H_2 or hydrocarbon depending on fuel processor
[2]Syn gas consists of H_2 with H_2O, CO, CO_2, depending on cell type

Figure 9.1 A complete fuel cell system consisting of subsystems for chemical to electrical energy conversion and thermal management.

accommodate reforming or direct oxidation of the sulfur-free fuel within the stack. The oxidation of this fuel within the fuel cell stack produces exhaust that consists of water and carbon dioxide, given that the primary fuel is a hydrocarbon. Emissions of sulfur oxides are very low because sulfur is removed upstream of the fuel cell, and emissions of nitrogen oxides are very low because reactions in both the fuel processor and the fuel cell occur over catalysts at temperatures <1000°C. Furthermore, while fuel cells operating on reformed hydrocarbons do produce carbon dioxide, the emissions are lower than for other less efficient energy conversion technologies.

The *fuel cell stack* is composed of series-connected fuel cells, each of which is supplied with fuel and air and produces direct current at less than one volt. The entire stack voltage ranges from a few volts to a few hundred volts, depending on the number of cells connected in series. The stack voltage decreases gradually as the load current increases until it reaches a limit determined by mass transfer restrictions. A *power management system* is required to regulate the stack voltage to match the load, prevent transient power demands that could damage the stack, and control the system output voltage to meet the needs of the application. While the fuel cell system is efficient relative to traditional engines, roughly half of the input chemical energy is still transformed to thermal energy, which leaves the stack in the exhaust gas, or, for low-temperature cells, in the stack cooling fluid. The *thermal management system* uses this thermal energy within the fuel cell system to preheat fuel and air or supplies the thermal energy externally for cogeneration

applications. Finally, depending on system characteristics, the *water management system* may use water for humidifying air and fuel or for reforming fuel, and may acquire this water from external sources or recover it from the stack exhaust. The requirements associated with these six systems are determined by the application and by the selection of the fuel cell technology utilized within the stack.

9.2 DIFFERENT FUEL CELL TECHNOLOGIES

Different fuel cell technologies are categorized by the nature of the application and the desired fuel source. The basic components of a fuel cell shown in Figure 9.2 include an anode where fuel is oxidized; a cathode where oxygen is reduced; collector plates, which connect the electrodes to the external load and provide flow channels for conveying products and reactants; and an electrolyte that transports ions between the electrodes. Fuel cell technologies can be classified by the type of electrolyte, fuel source, operating temperature, or application, but the operating temperature is perhaps the most important distinguishing feature, as it affects all of the other characteristics.

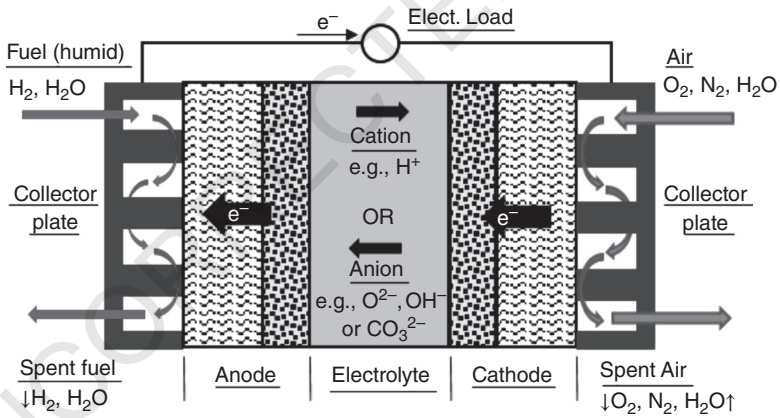

Notes:

1. The MCFC reactions involving CO_3^{2-} also require CO_2 at the cathode and yield CO_2 at the anode (not shown here)
2. SOFC and MCFC can also utilize simple hydrocarbon fuels such as methane through internal reforming or direct reaction at the anode

Figure 9.2 A typical fuel cell that includes two electrodes, anode and cathode, collector plates with embedded flow channels for supplying gas, and an electrolyte in the middle that separates the two electrodes while permitting ion transport. (*See electronic version for color representation of this figure.*)

9.2.1 Low-temperature Fuel Cells

Fuel cells designated as "low temperature" generally operate below 200°C. Low-temperature fuel cells typically exhibit high power density, rapid start-up, relatively simple and inexpensive assembly processes and materials (excluding catalysts), simple balance of plant components, and high electrical conversion efficiency. These characteristics align with the critical needs for automotive power systems and have made them, particularly the polymer electrolyte membrane (PEM) fuel cells, the target technology for this large market application. On the other hand, low-temperature operation means that catalysts are typically expensive platinum group metals (PGMs) and that fuel options are essentially limited to hydrogen and methanol. Furthermore, low-temperature operation precludes the use of waste heat for fuel processing operations and may limit the utility of thermal energy for cogeneration applications.

In the automotive application, heat for cabin comfort does not require high temperatures and onboard reforming is not a practical option, so low-temperature operation does not present significant disadvantages. Instead, the key impediments to widespread deployment of low-temperature fuel cells for automobiles are the high cost of the PGM catalyst, the inadequate durability of the membrane electrode assembly (MEA), and the lack of a hydrogen fueling infrastructure. To reduce or eliminate the need for expensive PGM catalysts, researchers are pursuing low-cost catalyst options and anion exchange membrane (AEM) fuel cells in which the oxygen reduction reaction (ORR) occurs in a more favorable alkaline environment.

Other applications for low-temperature fuel cells include small-scale stationary power and cogeneration applications, which utilize fuel cell systems operating at the upper end of the "low temperature" range (i.e., high-temperature PEM or HT-PEM) to provide both electricity and heat for buildings; and portable electronics where direct methanol fuel cells (DMFCs) show promise.

Polymer Electrolyte Membrane (PEM) Fuel Cells

The PEM fuel cell (PEMFC) uses a thin membrane fabricated from an acidic ion-conducting polymer (ionomer) as an electrolyte to conduct H^+ ions from the anode to the cathode. The typical membrane material consists of a polymer backbone that resembles PTFE with pendant side-chains terminated by perfluorosulfonic acid (PFSA) groups which, when the polymer is hydrated, create ionic transport pathways through the material [5]. Other ionomers have been developed as potential alternatives to the benchmark PFSA materials to improve durability and cost. These include modified fluoropolymers and non-fluorinated acid ionomers based on poly(arylene ether)s and polyimides [6]. A typical low-temperature ionomer can operate at temperatures up to approximately 100°C but must remain well-hydrated to achieve sufficient conductivity. Thus, the nature of the electrolyte establishes the fuel cell system temperature limit and requires that the balance-of-plant includes provisions for humidifying inlet fuel and air streams.

The overall PEM cell structure is similar to that shown in Figure 9.2 in which the PEM electrode consists of two distinct structures: the catalyst layer (CL), which

is adjacent to the membrane and provides the electrochemical reaction sites, and the gas diffusion media (DM), which provides a porous, electrically conductive path between the CL and the collector plate. At low temperatures in an acidic environment, the catalyst layer has historically required PGM catalysts to achieve sufficient electrochemical activity [7]. The catalyst is generally synthesized as nanometer-sized PGM particles decorated onto carbon particles ($d \sim 100$ nm) to create a carbon-supported catalyst. The carbon-supported catalyst, along with the ionomer, is dispersed in a solvent and cast onto the electrolyte membrane (or onto the surface of the DM) to form a porous structure with intermingled electrical and ionic pathways that connect the PGM catalyst sites to the electrolytic membrane and to the DM. Reactant gas from flow channels in the collector plates travels through the DM to the CL reaction sites and, at the cathode, the reaction product (i.e., water) diffuses back through the DM and is removed with the oxygen-depleted air.

As the cost and durability remain the two primary impediments to the widespread adoption of PEM fuel cells, key areas of development at the cell level include reduction of catalyst loading at the cathode, improved durability of the membrane and catalyst, and improved water management in the cathode. The PGM catalyst accounts for roughly 20% of the PEM fuel cell system cost, with the majority of the cost attributable to the cathode catalyst loading. Cost reduction focuses on decreasing the catalyst loading (presently 0.16 g/kW with a target of 0.125 g/kW), or eliminating the PGM catalyst entirely by replacing it with materials such as metal-nitrogen-carbon (MNC) catalysts, which have shown promising activity for the ORR [8–10]. The catalyst also presents a challenge for durability since, over time, the larger catalyst particles tend to grow or coarsen at the expense of smaller particles, leading to a loss in active area and reduced performance [11]. Corrosion of the carbon support can contribute to this coarsening effect [12]. Both catalyst coarsening and carbon corrosion are believed to be enhanced by voltage cycling caused by varying load conditions and by operation at high voltage idling conditions [11]. The catalyst life can be extended through the use of improved carbon or non-carbon supports and by better management of the operating environment of the cell (i.e., temperature, humidity, voltage) [11, 13]. Power electronics can contribute to PEM fuel cell durability by properly controlling the load transient and managing the cell voltage during start-up and shut-down. In addition to catalyst degradation, hydrothermal cycling of the membrane is believed to lead to membrane thinning and pinhole formation, with failure occurring when the membrane is no longer an effective barrier between the anode and cathode [14, 15]. Efforts to improve membrane durability include the development of more robust polymers and the use of composite materials [6]. Finally, the control of water, particularly in the cathode where water may condense and block the transport of oxygen to the catalyst sites, remains a challenge that limits the areal power density of PEM fuel cells [16–18]. Table 9.1 summarizes state-of-the art performance and cost metrics for the PEMFC alongside comparable metrics for other fuel cell technologies.

TABLE 9.1 Status and targets for key fuel cell system performance metrics.

	Transportation operating on H_2 80 kW		Residential operating on NG 1–25 kW		Distributed generation operating on NG 100 kW – 3 MW			
	2015 PEM[a]	Final target[a]	2015 PEM[a] and SOFC[a]	Final target[a]	2015 PEM[a]	2015 SOFC[a]	2015 MCFC[b]	2020 target[a]
Electrical efficiency (LHV)	60%	70%	34–40%	45%	42–47%		47%	50%
Cogeneration efficiency (LHV)	NA	NA	80–90%	90%	70–90%		84%	90%
Equipment cost, $/kW	53	30	2300–2800[c]	1500[c]	1200[d]	4500	4200[e]	1000
Durability, 1000 hours	3.9	8.0	40–70	60	40–80		40[e]	80
Power density,[f] W/liter	640	850	-	-	-	-	-	-

Notes:
a. Data from [8] unless noted otherwise.
b. Performance based on *SureSource 1500* by Fuel Cell Energy, Inc. [19].
c. Cost at production volume of 50,000 units per year.
d. Cost at production volume of 1000 units per year.
e. Cost and durability from [20, 21]; cost reported is 2010 cost at actual production volume of 30 MW/y.
f. Specific power is primarily relevant to the transportation application and is not a key metric for stationary applications.

Anion Exchange Membrane (AEM) Fuel Cells

One approach for reducing the catalyst cost in low-temperature fuel cells is to operate the fuel cell electrodes in an alkaline environment in which a variety of less expensive catalysts (e.g., inorganic oxides, Fe, Co, Ag, and others) can be used [22]. The alkaline environment also allows the use of less expensive materials for the collector plates and may be more favorable for the oxidation of some alcohol fuels [23]. Alkaline fuel cells (AFCs) were employed in the US Apollo spacecraft in the 1960s and later in the Space Shuttle Orbiter. In these stacks, the electrolyte was a liquid KOH solution with OH^- as the mobile ion, moving from cathode to anode [24]. The liquid electrolyte was retained in a porous matrix and further constrained between the two porous electrodes. Today, research is focused on replacing the liquid electrolyte with an AEM to provide a polymeric electrolyte with OH^- mobility, thus avoiding the difficulties associated with retaining the liquid electrolyte.

A variety of options have been considered for the AEM material, which generally consists of a cationic group (e.g., quaternary ammonium) attached directly or via a sidechain to a polymer backbone (e.g., poly(arylene)ether)) [22]. The cationic groups form conductive pathways through the membrane for OH^- ions. The challenges for AEM fuel cells (compared with PEM fuel cells) arise from the relatively poor stability of the AEM material and the lower mobility of the OH^- ion, which leads to higher ohmic losses in the membrane. Furthermore, the presence of CO_2 in the cathode air supply enables the formation of CO_3^{2-} and HCO_3^- ions. In liquid electrolyte alkaline fuel cells, these ions combine with the mobile cation (K^+ or Na^+) to form solid precipitates. For AEMs, the cation is bound to the polymer backbone, thus precluding the formation of precipitates. However, the CO_3^{2-} and HCO_3^- ions can accumulate in the membrane, particularly at the anode, and reduce the cell performance [22]. By removing CO_2 from the air or by using oxygen at the cathode, several studies have demonstrated the operation of AEM fuel cells at practical power densities using PGM-free catalysts [25, 26]. However, more research and development will be required to realize the goal of PGM-free AEM fuel cells with performance approaching that of the PEM fuel cell.

Phosphoric Acid Fuel Cells (PAFCs)

The PAFC is typically designated as a high-temperature PEM (HT-PEM) fuel cell. The first large-scale commercial deployment of fuel cells used PAFC technology. These systems employed an H^+ conducting electrolyte as in the modern PEM fuel cell, but instead of a polymer, the electrolyte was a porous silicon carbide matrix infused with phosphoric acid. These cells operated at temperatures as high as 200°C and exhibited sufficient durability (some systems exceeded 40,000 h of operation) to be used in megawatt-level distributed generation and stationary cogeneration applications, with more than 500 units installed worldwide [27, 28]. Unfortunately, this generation of phosphoric acid fuel cells exhibited low power density and required relatively high PGM loadings (with corresponding high cost), making them unattractive for transportation applications and limiting their widespread use

even in stationary applications. More recently, techniques have been developed to infuse a high-temperature polymer such as polybenzimidazole (PBI) with phosphoric acid to form an H^+ conducting polymer composite suitable for operation at temperatures of 150–200°C [29]. These PBI/phosphoric acid membranes are also attractive because they do not require moisture for operation, thus eliminating the water management and humidity control issues associated with PEM fuel cells using PFSA membranes. The HT-PEM is particularly promising for cogeneration applications where the higher operating temperature (>150°C) not only provides more useful thermal energy but also makes the anode catalyst tolerant of up to 1% CO. For stationary applications using hydrocarbon fuels, greater CO tolerance may eliminate the need for a final CO cleanup operation in the fuel processor, thus reducing cost and complexity. Major challenges with HT-PEM systems, relative to PEM systems based on PFSA membranes, include insufficient durability, higher catalyst loadings, and lower power density [29].

Direct Methanol Fuel Cells (DMFCs)

The DMFC configuration is similar to that of the PEM fuel cell, but instead of hydrogen, the DMFC uses a dilute methanol solution as the fuel at the anode. As a liquid, methanol has a much greater energy density than that of hydrogen, and in relatively small systems has a greater specific energy when the complete storage system is considered. **Table 9.2** compares the specific energy and energy density between hydrogen gas and other fuels [30]. The use of methanol also simplifies transportation and refueling operations. Unfortunately, the methanol oxidation reaction at the anode is quite slow, thus leading to low power density and the need for high loadings of PGM catalysts. Furthermore, the membranes (e.g., PFSA ionomers) used in the DMFC permit methanol crossover which reduces the fuel cell efficiency. The crossover can be mitigated by using more dilute methanol solutions (e.g., 3–10 wt% methanol in water), but then the gravimetric and volumetric advantages of methanol are reduced. This problem can be overcome by storing methanol at high concentration and then mixing the stored fuel with water (recovered from the cathode reaction) prior to introduction to the anode. Crossover can also be reduced by feeding the methanol solution to the anode as a vapor. Techniques to dilute and vaporize methanol increase the system complexity, but in many cases the system can still be implemented passively (i.e., without the benefit of pumps,

TABLE 9.2 Comparison of hydrogen and other fuels for their specific energy and energy density.

Fuel type	Pressure (bar)	Specific energy (MJ/kg)	Energy density (GJ/m^3)
Hydrogen, H_2/metal hydrides	14	142	3.6
Ammonia, pressurized tank	10	22.5	13.6
Methanol, CH_3OH/liquid tank	1	15.2	11.4
Gasoline, C_8H_{18}/liquid tank	1	46.7	34.4

sensors and controls) [31]. Another approach for limiting crossover is to develop new or modified membrane materials that maintain high H^+ conductivity while exhibiting low methanol permeability, though these characteristics generally conflict with one another [32].

In addition to limiting fuel crossover, methanol systems must be designed to manage the evolution and transport of CO_2 gas, which is produced by the methanol oxidation reaction at the anode. The structure of the electrode and fuel supply system must accommodate a liquid/gas mixture and must vent the gas phase to the surroundings [33]. These requirements further reduce the power density and complicate the fuel supply system.

Thus, in spite of the advantages offered by a liquid fuel, the low power density, poor efficiency, and high cost of the DMFC have made it unattractive for high-power applications. Instead the DMFC is primarily considered for low-power applications that require extended operating periods, such as portable electronics. Systems for these types of applications have been demonstrated at sizes ranging from 1–100 W [31]. Widespread application of DMFC technology in these portable power applications will likely require the development of novel membranes that provide H^+ conductivity while limiting methanol crossover.

Direct Ammonia Fuel Cells (DAFCs)

As shown in **Table 9.2**, ammonia has a much higher energy density than hydrogen under the same or less pressurized condition. In addition, ammonia is a carbon-free gas and its reforming process does not emit CO, CO_2, or any other hydrocarbon. These characteristics of high energy density and zero-carbon together with low cost and the appeal of a liquid fuel have encouraged interest in ammonia as a clean energy carrier to replace hydrogen, especially in transportation applications [30, 34–36].

Early studies envisioned the use of ammonia as a direct fuel for elevated-temperature alkaline fuel cells or for high-temperature solid oxide fuel cells. A reforming process to convert ammonia to hydrogen was generally considered essential for the use of ammonia in low-temperature fuel cells. However, a recent study has demonstrated the feasibility of using low-temperature (<200 °C) fuel cells with direct ammonia [34]. Under low pressure and ambient conditions, the direct ammonia fuel cell (DAFC) holds 6 kWh/kg specific energy, much higher than the 1.7 kWh/kg held by compressed hydrogen at 700 bars. Unfortunately, ammonia is toxic and flammable and the technology required for safe handling and storage tends to increase the overall cost.

Prospects and Challenges for Low-temperature Fuel Cells

Technology for PEMFCs, based on PFSA membranes, has improved dramatically over the last two decades and seems likely to approach key performance targets through evolutionary design and manufacturing process development. Revolutionary advances that could encourage adoption of PEMFC technology include the development of durable PGM-free catalysts for the oxygen reduction reaction

(ORR) and CO-tolerant hydrogen oxidation reaction (HOR) catalysts. The former could, by itself, cut the gap between current and targeted PEMFC system costs in half. The latter would significantly lower the cost of fuel processing for stationary applications (discussed in a subsequent section), thus facilitating a gateway market that would help move PEMFC technology forward. Other low-temperature technologies are considerably more high risk/high reward. Technology for AEM fuel cells is appealing for catalyst cost reduction and fuel flexibility, but low OH^- conductivity in fuel cell conditions and limited durability are quite challenging. Likewise, while HT-PEM technology is conceptually appealing, the pathways for overcoming high catalyst cost, low power density, and durability challenges are not clear.

9.2.2 High-temperature Fuel Cells

High-temperature (i.e., operating at >500 °C) fuel cells include solid oxide fuel cells (SOFCs) and molten carbonate fuel cells (MCFCs). The SOFC typically operates in the range of 700–1000 °C, with ongoing development efforts to lower the temperature to as low as 500 °C. The SOFC comprises a porous ceramic-metal (cermet) composite anode, a dense O^{2-} conducting ceramic electrolyte, and a porous ceramic cathode [37]. The MCFC operates at a temperature of approximately 650°C and is fabricated primarily from metallic components with a molten salt electrolyte that is retained within a porous structure.

Sufficiently high operating temperatures may permit the direct electrochemical oxidation of methane at the fuel cell anode. Even at somewhat lower temperatures, thermal energy from the electrochemical reaction can be used in an upstream fuel processor to reform ammonia, methane and other hydrocarbons to produce hydrogen, which can then react electrochemically at the anode. High operating temperatures also eliminate the need for precious metal catalysts because the ORR can proceed at a sufficient rate without a catalyst at SOFC temperatures and on the surface of inexpensive nickel oxide catalysts at MCFC temperatures, and the HOR proceeds without a catalyst in the SOFC and on nickel catalysts in the MCFC. Reforming of hydrocarbon fuels, though, requires catalysts that range from low-cost industrial catalysts such as nickel for steam-reforming of natural gas, to more exotic catalysts for reforming heavier hydrocarbons. In addition to fuel flexibility and low-cost catalysts, high-temperature fuel cells offer the advantage of yielding high-temperature thermal energy that can be used for cogeneration systems that simultaneously produce electricity and heat for buildings or industrial processes.

In general, high-temperature fuel cells exhibit lower areal specific power, higher cost, and slower start-up/shut-down processes relative to low-temperature fuel cells. For both SOFC and MCFC, high ohmic resistance associated with the electrolyte requires relatively low current density and hence requires large cell areas and large stacks. This large stack size requirement leads to high costs despite the absence of precious metal catalysts. High-temperature fuel cells can also experience thermal gradients or mismatches in expansion coefficients for fuel cell components that can lead to stresses within the stack. These stresses can fracture the

stack materials, particularly the relatively brittle materials in the SOFC. Stresses can be exacerbated by rapid changes in temperature, thus necessitating slow start-up/shut-down processes. In addition, the need to purge the reactants from the stack by using inert gas introduces additional complexity in the start-up/shut-down operations. The system complexity is further increased by the incorporation of the fuel processing steps necessary to accommodate fuels other than hydrogen.

Large stack size and increased balance of plant complexity typically make the overall system size much larger for high-temperature fuel cell systems than for low-temperature systems of comparable power. The combination of larger sizes, higher cost, and the need for continuous operation make high-temperature cells a better fit for distributed generation applications than for portable power or transportation power. Furthermore, the advantages of high-temperature systems – use of widely available fuels like natural gas and availability of heat for cogeneration – also make them attractive candidates for distributed generation.

Solid Oxide Fuel Cells

Research interest in SOFCs accelerated in the 1980s with the introduction of the Westinghouse tubular SOFC design [38]. In this design, a porous, electrically conductive support tube is surrounded by concentric layers comprising the cathode, electrolyte, and anode. A nickel–felt interconnect is passed through the electrolyte and anode to provide a series-connection between the interior cathode of one tube and the exterior anode of the adjacent tube. In contrast to the planar structure shown in Figure 9.3a, the tubular structure shown in Figure 9.3b simplifies fabrication, interconnection, and sealing issues and tends to be more resistant to damage arising from thermal gradients within the stack. On the other hand, the power density (kW-m^{-3}) of the tubular stack is lower, making costs higher. Though tubular designs are attractive in some applications [39], the planar configuration tends to be more common [40].

The SOFC anode is a cermet which is chosen based on a number of requirements including the ionic and electronic conductivity, fuel composition, operating

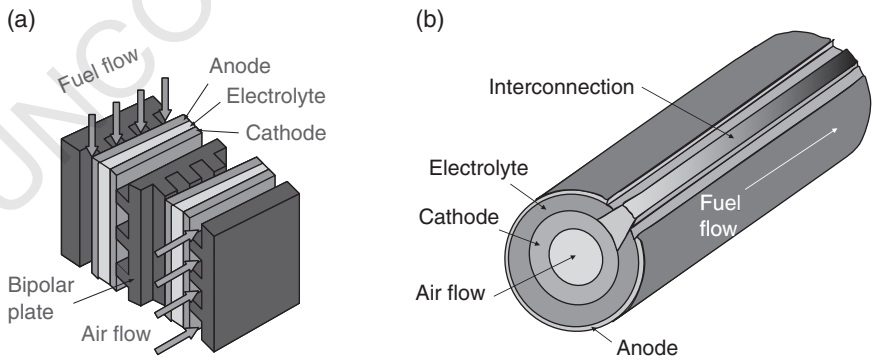

Figure 9.3 Fuel cell stack structures: (a) planar; and (b) tubular. (*See electronic version for color representation of this figure.*)

temperature, and thermal expansion considerations, among others, and is commonly a mixture of the ion-conducting ceramic, yttria-stabilized zirconia (YSZ), with alloys of Ni or Cu. With a properly designed anode, the SOFC is capable of oxidizing hydrogen, synthesis gas mixtures (derived from gasification of solids or external reforming of natural gas) and natural gas itself [41]. Natural gas is of particular interest, and can in theory be oxidized directly (dry) on the anode or mixed with water to accomplish internal steam reforming within the SOFC stack. This fuel flexibility is among the most significant advantages of the SOFC. Fuel oxidation within the anode yields a mixture of H_2O, CO_2, and unreacted fuel (typically 15% or more depending on the application) at the anode exit [42]. The unspent fuel can be oxidized to produce heat for fuel reforming, or combusted in a downstream gas turbine (GT) in hybrid SOFC/GT systems. If the anode exit gas is reacted with pure oxygen, the final exhaust will consist of H_2O and CO_2, from which the H_2O can be condensed to yield a stream of concentrated CO_2. This CO_2 stream can be captured and sequestered much more economically than the CO_2/excess air mixture from a combustion process.

The electrolyte is a key determinant of cell performance for the SOFC because, at high temperatures, activation losses are small and the voltage drop associated with ion transport through the electrolyte dominates the cell performance. The ionic conductivity of SOFC electrolytes is very low at room temperature but increases with temperature. Early electrolyte materials (e.g., YSZ) required high temperatures and low current density to achieve acceptable performance. Advances in electrolyte materials and improved fabrication techniques that enable thinner electrodes have allowed designers to pursue a lower operating temperature and/or a higher current density. The former choice (lower temperature) helps to minimize the balance-of-plant costs, facilitate operational cycling, and improve durability, while the latter choice reduces stack cost. Today, several electrolyte materials are available based on the desired operating temperature, including YSZ (~700 °C), strontium, magnesium-doped lanthanum gallate (~550 °C), and gadolinium- or samarium-doped ceria (~550 °C) [41]. However, operation at temperatures below 600 °C begins to impact the fuel flexibility and the thermal integration with the upstream fuel processor.

The SOFC cathode is a mixed ion/electron conducting ceramic chosen to provide excellent electrical conductivity, compatibility with the electrolyte, high electrochemical activity for the ORR, porosity for oxygen transport, and high thermal stability. Perovskites (e.g., lanthanum, strontium, manganite), are commonly used as cathode materials and may be mixed with electrolyte materials (e.g., YSZ) to provide ionic conductivity and to enhance the availability of gas/electrolyte/electrode interfaces where the ORR occurs [41].

Research and development of SOFC systems is presently focused on improved materials and better manufacturing processes that can yield lower operating temperatures, lower cost, and improved durability. Considerable progress has been made, with estimated high-volume production costs dropping from $1500 to $175 per kW over the 2000–2010 period, and stack degradation as low as 0.3% per

1000 h reported for recent stack designs [40]. Table 9.1 summarizes state-of-the-art performance and cost metrics for the SOFC alongside comparable metrics for other fuel cell technologies.

Molten Carbonate Fuel Cells

Molten carbonate fuel cells were demonstrated at commercial sizes in the early 1990s, and since that time more than 80 MCFC systems have been installed in locations around the world with a combined capacity of more than 300 MW [43]. The MCFC operates at roughly 650 °C and consists of a planar configuration that includes a porous nickel-aluminum anode, an electrolyte composed of a mixture of lithium carbonate and potassium (or sodium) carbonate retained in a porous lithium aluminate matrix, and a porous lithiated nickel oxide cathode [20]. Fuel (e.g., hydrogen and carbon monoxide) is supplied to the anode where it reacts with carbonate ions from the electrolyte to produce water and carbon dioxide. Air and carbon dioxide are supplied to the cathode where the oxygen is reduced to form carbonate ions (CO_3^{2-}) that travel through the electrolyte to the anode. The CO_2 supplied to the cathode is typically obtained by recycling a portion of the anode exhaust gas. The need for CO_2 at the cathode is unique among fuel cells and introduces additional complexity for MCFC systems. Recently, CO_2 capture systems have been proposed to exploit this feature by supplying flue gas from a fossil-fuel power plant to the MCFC cathode. Excess air in the flue gas combined with supplemental air then supplies the oxygen for the ORR, while the cathode CO_2 is supplied by the combustion products in the flue gas. In this design, the CO_2 from the fossil-fuel plant is captured in the carbonate ion and transported to the anode where it reacts with the fuel to produce CO_2 in the anode exhaust stream. The advantage that this offers is that the CO_2 is removed from the dilute flue gas and introduced into the concentrated anode exhaust stream from which it can be more easily removed, thus avoiding the need for expensive and maintenance-intensive CO_2 scrubbing from the flue gas. These MCFC-enabled CO_2-capture systems are in the early stages of research and development [43].

Since the MCFC operates at ~650 °C and uses a relatively benign electrolyte, it can be manufactured with collector plates fabricated from inexpensive stainless steel (with nickel cladding at the anode) [20]. The use of low-cost materials for the collector plates and electrodes is a cost advantage; however, this is offset by a relatively low areal power density (ca. 150 mW-cm^{-2}), which leads to large fuel cell stacks. The operational limits imposed by a molten liquid electrolyte, the system complexity introduced by the need for CO_2-recycle, and the large stack size make the MCFC system unattractive for small power applications. On the other hand, the MCFC exhibits excellent durability, with 40,000 operational hours demonstrated and 80,000 hours targeted [20]. Further, the high operating temperature allows the integration of fuel reforming within the stack or in a thermally integrated external fuel processor, allowing the system to be fueled by simple hydrocarbons such as natural gas and biogas. Currently, the MCFC is commercially available in sizes of 300 kW, 1.4 MW, 2.8 MW, and 3.7 MW [19], with recent estimates indicating an

installed cost of $4200/kW for a natural gas fueled system [20]. Thus, for large stationary applications, the MCFC offers the advantages of high efficiency, low emissions, fuel flexibility and durability, but these advantages come at a cost premium relative to other distributed generation options (e.g., internal combustion engines with an installed cost of roughly $1500/kW).

Prospects and Challenges for High-temperature Fuel Cells

Technology for SOFCs shows significant promise for cogeneration systems and advanced cycles (e.g., SOFC/GT cycles). While progress toward cost and durability goals has been slower than originally anticipated, recent estimates of high-volume stack production at costs as low as $175/kW and several reports of degradation lower than 1% per 1000 hours are very encouraging. Furthermore, the availability of low-cost natural gas is very favorable for the deployment of SOFC distributed generation systems. Key remaining challenges include the development of materials with improved durability, the development of materials and designs that achieve lower temperatures and higher power density, and the development of manufacturing approaches that are economical at the relatively small production scales associated with initial markets. In contrast to SOFC technology, MCFC technology has been relatively stable for a long period. The durability of the MCFC is impressive and it does offer the prospect of integration with carbon sequestration systems. However, it is difficult to see how MCFC technology will compete over the long term with SOFC technology, which is likely to become considerably less expensive.

9.3 FUEL CELL APPLICATIONS

The successful deployment of fuel cell technology will require that the fuel cell system provides a significant benefit over existing technologies. Currently transportation and stationary power generation are the two most promising opportunities for the adoption of fuel cell technology.

9.3.1 Transportation Applications

Since the emergence of the automobile at the turn of the twentieth century, scientists and engineers have been searching for electrochemical alternatives to the internal combustion engine as a power source for personal transportation. Early batteries (ca. 1900) were based on lead-acid technology and provided limited power and range. Electric vehicles powered by improved lead-acid and nickel metal hydride batteries were aggressively explored again in the 1990s, but were ultimately unable to meet consumer needs at an affordable price. Fuel cell electric vehicles (FCEVs) emerged as a transportation alternative in the late 1990s, with the development of the PEM fuel cell with its high power density, efficiency, and low operating temperature, which facilitated rapid start-up. USCAR, a consortium of major automobile manufacturers, launched the FreedomCar initiative in 2002 to

encourage the development of FCEVs [44]. Initially, fuel cell technology advanced rapidly with improvements in performance, system integration and cost. However, durability challenges, slow deployment of a hydrogen infrastructure, limited progress with onboard hydrogen storage, and persistently high cost estimates, due in large measure to the use of Pt catalysts, led to waning research and development funding by the late 2000s. In addition, the emergence of the lithium ion battery (LIB) as a potential alternative for transportation led some to question the viability of fuel cells. In 2011, the FreedomCar initiative transitioned to US DRIVE with a broader portfolio of technologies including, among others, both fuel cells and advanced vehicle batteries [44]. Today both fuel cells and LIBs are considered viable candidates for meeting the demands for future personal transportation, with range requirements, cost, and availability of hydrogen infrastructure likely to be the deciding factors in the success of one or the other (or both) technologies [45, 46].

An analysis by Gallagher et al. suggests that advanced lithium batteries (e.g., silicon/carbon composite anodes with high-energy nickel manganese cobalt (NMC) cathodes) may achieve specific energy values as high as 250 Wh/kg, corresponding to roughly twice the specific energy of current state-of-the-art LIBs [47]. Battery technologies such as pure lithium anodes and lithium-oxygen batteries may offer even higher values for energy density, but the development challenges for these technologies are quite high and not likely to be solved in the near future. Groger, Gasteiger, and Suchsland provided an analysis of range and cost for vehicles powered by advanced lithium batteries (i.e., with specific energy ~250 Wh/kg or about double that of current batteries). They concluded that "without radical changes in battery and/or vehicle technology, the production of battery electric vehicles with driving ranges of ~200 miles might be challenging and for anywhere near 300 miles is likely not feasible for the mid-size car market due to battery weight and cost constraints" [45]. Larger vehicles and longer ranges are likely to be very difficult to achieve, even with more advanced lithium batteries, unless the vehicle is hybridized (e.g., Chevy Volt, Toyota Prius Plug-In).

Against this backdrop, the FCEV offers the potential for larger size, lower cost for long-range vehicles, and rapid refueling. Currently available FCEVs include the 2017 Honda Clarity (mid-sized sedan), 2017 Hyundai Tucson Fuel Cell (small SUV) and Toyota Mirai (sub-compact sedan), which are available for lease-only in limited markets where a hydrogen infrastructure is emerging, such as Japan and parts of southern California [48]. The range, power and refueling time for these FCEVs have been shown to be comparable to gasoline vehicles. However, since these vehicles are lease-only, manufactured using small-scale production, and intended for demonstration purposes, they provide limited insight into the economics of fuel cell technology. Most considerations of fuel cell cost reference the US Department of Energy's (DOE) Hydrogen and Fuel Cell Multi-year Research Development and Demonstration Plan (MYRDDP), which has established cost targets for FCEV implementation and has tracked progress against these targets since 2002 [8]. As noted in Table 9.1, the current cost (based on 500,000 vehicles per year production rate) is estimated to be $53/kW with a long-term goal of $30/kW.

The current cost estimate reflects an impressive 75% reduction from the 2002 cost estimate of $200/kW [49]. For an 80 kW-net fuel cell system, combined with a 5 kg, 70 bar hydrogen storage tank (sufficient for 300 miles), the long-term cost targets yield a system cost of approximately $4900, which compares favorably with the $21,000 advanced lithium battery system required to achieve the same range [45].

While the FCEV offers size, range, refueling rate, and at least the prospect of reasonable cost, challenges remain in the areas of durability and hydrogen infrastructure. Currently, as indicated in Table 9.1, durability in typical vehicle applications is estimated to be about half of the necessary 8000 hours. As noted previously, catalyst degradation and membrane damage represent key impediments to longer life, with the power management system playing a key role in managing the cell voltage to limit damaging cell potentials during dynamic operation. In the area of infrastructure, an enormous investment will be required to implement a hydrogen refueling network large enough to allow the widespread adoption of FCVs. In the near term, this is likely to limit FCVs to captured fleets (e.g., taxis, service vehicles, etc.) or to high-density population centers where the infrastructure is more economical. More widespread application may require smaller, cheaper, less complex refueling stations. Key enabling technologies for these stations are likely to be low-cost electrolyzers and advanced hydrogen storage technologies that allow vehicles to store hydrogen at lower pressures (<100 bar), thus reducing the cost of hydrogen compression and dispensing systems.

The environmental impact of large-scale FCEV deployment depends on the scope of the analysis and the origin of the hydrogen fuel. Locally, hydrogen-fueled FCEVs are environmentally benign, producing only water as a tailpipe emission, and eliminating emissions of CO_2 as well as all of the criteria pollutants (i.e., particulates, oxides of sulfur, oxides of nitrogen, carbon monoxide, unburned hydrocarbons) associated with internal combustion engine (ICE) vehicles. Globally, the impact of the FCEV on CO_2 emissions depends on whether the hydrogen is produced by reforming natural gas or by electrolyzing water.[1] Natural gas reforming is the most common approach for industrial production of hydrogen, and yields CO_2 in proportion to the carbon content in the natural gas. For the same amount of energy, natural gas has a lower carbon content than petroleum fuels. Furthermore, FCEVs operate with a higher efficiency, particularly at part-load, than ICE vehicles. On the other hand, compression and distribution of hydrogen is more energy-intensive than distribution of petroleum fuels. Electrolysis is currently a more expensive and less common method for producing hydrogen, and the global emissions depend on whether the electricity is produced by a typical utility mix of generating resources or whether the electricity is derived from renewables.

A well-to-wheels analysis suggests that FCEVs emit 50% less CO_2 than using ICEs fueled by gasoline when the hydrogen for the FCEV is produced by steam methane reforming and stored onboard as compressed hydrogen. If hydrogen is

[1]Electrolysis achieves the opposite result of the fuel cell reaction in a similarly configured device. In electrolysis, water enters the electrolyzer and an electrical current is used to drive oxygen evolution at one electrode and hydrogen evolution at the other.

produced by electrolysis and the electricity source is the US average mix of generating resources, then FCEVs yield roughly 20% more CO_2 than gasoline ICE vehicles. However, if the electricity is from renewables (i.e., hydro, solar or wind) or nuclear, then both local and global FCV emissions are negligible [50].

9.3.2 Stationary Power Generation Applications

The prospects for the use of fuel cells in stationary power applications are, in many respects, more promising than in transportation applications because the technical and economic constraints are less demanding. Stationary fuel cell systems are generally fueled by natural gas and designed to provide 1–25 kW for single and multi-family residences (micro-cogeneration) and 100 kW–3.0 MW for commercial and utility systems. In contrast to transportation applications, the weight and volume constraints for these systems are not as stringent, and system costs as high as $1000/kW for natural gas fired systems can be economically attractive. The primary competing technology at very small sizes (<25 kW) is the small-scale internal combustion engine (ICE), which is not well suited for long-term continuous operation and which has relatively high maintenance costs. At larger scales, automobile or diesel derivative engines and micro-turbines are the primary competition and also suffer from relatively high maintenance requirements.

To compete with conventional systems at the small scale (1–25 kW), the US DOE 2020 targets presented in Table 9.1 specify a fuel cell system cost for large-scale production (i.e., 50,000 units per year) of $1000/kW and an operating lifetime of 80,000 hours [48]. Similar costs and durability are targeted for larger systems at smaller production scales. Some researchers argue that these targets are overly ambitious and that a more reasonable cost goal is roughly $3000/kW [51]. For current technology at current production volumes, costs are much higher and lifetimes lower than targeted, and yet several aggressive demonstration programs have been implemented. The largest demonstration program is the Japanese Enefarm program, an effort of the Japanese government, utilities, and fuel cell manufacturers, which as of 2012 had been involved in the installation of more than 20,000 micro-cogeneration systems. The 2012 price of these 700 W PEMFC-based systems was roughly $21,000 before subsidies. Japan, in conjunction with Osaka Gas, has also supported a large demonstration project for 700 W SOFC-based micro-cogeneration systems [52]. In addition to the micro-cogeneration systems widely demonstrated in Japan, other cogeneration systems have been demonstrated at various sizes ranging from a few kW to 3.0 MW. These systems have employed PEMFC, HT-PEM, MCFC, and SOFC technologies.

A primary advantage of the high-temperature fuel cell based stationary power systems is that cogeneration – the simultaneous on-site generation of power and thermal energy – makes better use of primary energy resources than centralized power generation. In a typical centralized coal-fired power plant, 60–65% of the chemical energy supplied in the fuel is discharged to the environment due to conversion losses without providing any useful benefit. Even for the newest

combined cycle power plants, roughly 40% of the input energy is discharged at the power plant. Furthermore, transmission and distribution losses lead to another 5–10% loss. On-site cogeneration allows the input fuel energy to be converted to electricity while allowing the thermal energy arising from conversion losses to be used for space heating or water heating. Cogeneration systems are commonly characterized by both an electrical efficiency and a cogeneration efficiency defined respectively as:

$$\eta_{el} = \frac{\dot{W}_{sys}}{\dot{m}HV} \tag{9.1a}$$

$$\eta_{cogen} = \frac{\dot{W}_{sys} + \dot{Q}}{\dot{m}HV} \tag{9.1b}$$

where $\dot{W}_{sys}$ is the power provided by the system (J-s^{-1}), $\dot{m}$ is the mass flow rate of fuel (kg-s^{-1}), HV is the heating value of the fuel (J-kg^{-1}), and $\dot{Q}$ is the thermal output rate available from the system (J-s^{-1}), while other variables are as previously defined. The cogeneration efficiency is somewhat misleading since the thermal output supplied by the system is worth considerably less economically (and thermodynamically) than the power output, but the metric is still commonly used. For natural gas fired cogeneration systems, typical values for electrical efficiency are 30–40%, and typical values for cogeneration efficiency are 70–90%.

For a fuel cell generation system that contains a fuel reformer, the fuel cell stack efficiency improves with decreasing load, but the reformer efficiency decreases with decreasing load as heat loss from the reactor vessels becomes relatively more significant. The combination of these two effects makes both the electrical and cogeneration efficiency relatively constant across a wide range of operation.

Another important consideration related to the efficiency metrics for a cogeneration system is that they indicate the fraction of the fuel input that is *available* from the system as electrical and thermal energy. But, to be useful, the output energy streams have to be both available *and* needed. Further, since both thermal and electrical energy are related to the fuel flow rate, they vary together and may or may not be in the same proportion as the thermal and electrical needs of the facility. For example, if the cogeneration system is operated to meet the electrical demand (i.e., electrical load following operation) for air conditioning while the simultaneous space heating and water heating requirements are small, then the thermal energy is not fully utilized and the effective cogeneration efficiency is reduced. On the other hand, if the system is operated to meet the thermal load (i.e., thermal load following operation), which happens to be small, and generates little electricity, then supplemental electricity must be purchased from the electrical grid. The thermal and electrical loads of the building can be aligned with the energy outputs from the cogeneration system by a bi-directional grid connection that allows electricity to be sold to or purchased from the grid; by on-site batteries; and/or by

thermal storage in the form of a variable-temperature water tank. The proper design of a cogeneration system can be quite complicated and requires consideration of the electrical and thermal load profiles, the system electrical and cogeneration efficiency metrics, storage options, and utility pricing structures. For the Japanese Enefarm demonstration program, the micro-cogeneration systems were sized to meet only a fraction of each residence's electrical power demand, with grid interconnection and thermal storage used as necessary to maximize the use of both the electrical and the thermal outputs.

In contrast to transportation applications where the environmental effects depend on the fuel source, stationary applications are almost always environmentally attractive. First, stationary fuel cell systems use natural gas, which has a lower carbon content and yields fewer emissions of criteria pollutants than the average US utility fuel mix, which typically includes coal, natural gas, and some nuclear. Second, stationary fuel cells convert fuel to electricity at the point of use with a greater efficiency than the average power plant can generate and distribute electricity.[2] Finally, the heat available from a fuel cell cogeneration system offsets the use of other fuels that would be combusted to meet the coincident heating load. Thus, stationary fuel cell systems reduce overall energy use and associated emissions when compared with energy systems based on conventional centralized power plants. The magnitude of the environmental benefit depends significantly on the effective cogeneration efficiency.

9.4 ELECTRICAL CHARACTERISTICS

9.4.1 Steady-state Operation

The steady-state electrical characteristics of a fuel cell are typically expressed in a polarization curve, similar to that shown in Figure 9.4 that relates voltage to current. The theoretical open circuit voltage is determined by thermodynamics and is a function of the cell temperature, the cell pressure, the type of fuel, and the concentrations of fuel in the anode and oxygen in the cathode. For a single fuel cell operating on hydrogen and air at atmospheric pressure, the theoretical open circuit voltage ranges from approximately 1.2 V for a PEM fuel cell at 80°C to approximately 1.0 V for a SOFC at 700°C. The actual open circuit voltage is somewhat less due to fuel crossover from the anode to the cathode. Referring to Figure 9.4, the initially steep drop in voltage associated with increasing current for the PEM fuel cell is attributable to the *activation overpotential* required to sustain the rate of the electrochemical reaction. Because of the high operating temperature, the activation overpotential is lower for the SOFC. As the current continues to increase, an *ohmic overpotential*

[2]Modern combined cycle power plants have a higher generating efficiency (e.g., ~60%) than stationary fuel cell plants, but the average electrical efficiency over all generating plants remains in the 35–40% range.

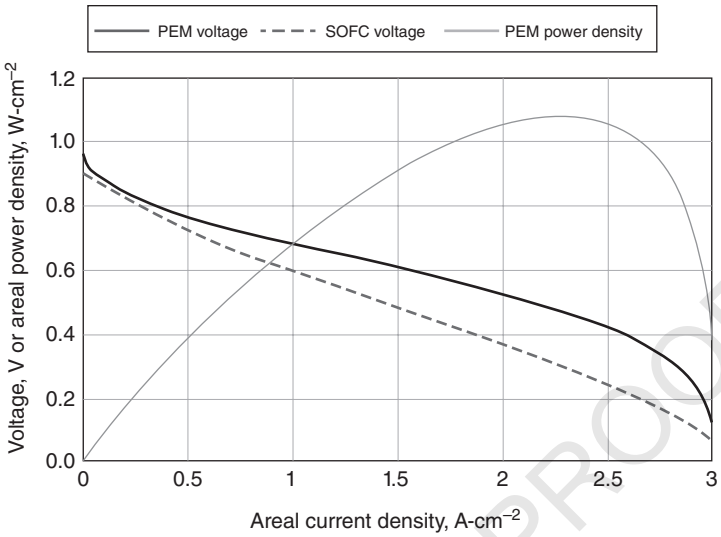

Figure 9.4 Polarization curve of a fuel cell depicting a steady-state relationship between voltage and current. (*See electronic version for color representation of this figure.*)

associated with the transport of ions through the electrodes and electrolyte and the transport of electrons through the electrodes and collector plates also becomes significant, causing the voltage to decline linearly with current over a broad range. Finally, as the current approaches high values, the concentration of reactants in each electrode decreases due to mass transfer limitations through the porous electrode, leading to a *concentration overpotential* that eventually drives the cell voltage to zero. The concentration overpotential is high for the PEMFC due to the formation of liquid water at high current, which impedes oxygen transport through the electrode.

The power provided by the cell is simply the product of voltage and current and, as shown for the PEM fuel cell in Figure 9.4, reaches a maximum at a current density roughly corresponding to the onset of significant concentration overpotential. The ideal electrical efficiency, η_{ideal} of the cell can be expressed as the ratio of the work available from the reaction (given by the change in Gibbs energy, ΔG (J-g^{-1}), for the reaction) to the heating value of the fuel, HV (J-g^{-1}):

$$\eta_{\text{ideal}} = \frac{\Delta G}{HV} \tag{9.2}$$

Multiplying the numerator and denominator by the mass flow rate of fuel, $\dot{m}$ (g-s^{-1}), and recognizing that the product of the mass flow and ΔG is the ideal power, $\dot{W}_{\text{ideal}}$ (W), yields:

$$\eta_{\text{ideal}} = \frac{\dot{m}\Delta G}{\dot{m}HV} = \frac{\dot{W}_{\text{ideal}}}{\dot{m}HV} = \frac{V_{\text{ideal}} I}{\dot{m}HV} \tag{9.3}$$

where V_{ideal} is the ideal or reversible voltage and I is the current. For fuel cells operating on hydrogen with minimal fuel crossover, the difference between V_{ideal} and the operating cell voltage, V_{cell}, reflects the sum of the overpotentials and thus the main inefficiencies associated with the cell.[3] The effect of these inefficiencies is captured in the voltage efficiency, η_V:

$$\eta_V \overset{\text{def}}{=} \frac{V_{cell}}{V_{ideal}} \tag{9.4}$$

The fuel cell electrical efficiency, η_{fc}, is the ratio of the fuel cell stack power, $\dot{W}_{fc}$ (W), to the flow of chemical energy into the stack and can be related to the ideal efficiency and the voltage efficiency:

$$\eta_{fc} = \frac{\dot{W}_{fc}}{\dot{m} \cdot HV} = \frac{V_{oc} I}{\dot{m} HV} \times \frac{V_{cell}}{V_{oc}} = \eta_{ideal} \times \eta_V \tag{9.5}$$

Eq. (9.5) implies that that the polarization curve also provides a good approximation of the variation of fuel cell efficiency with current. At high current, the cell efficiency suffers, while at part-load, the cell becomes more efficient as V_{cell} approaches V_{ideal}. This is in contrast to many other energy conversion devices for which the part-load efficiency is poor. Efficient performance at part-load makes fuel cells attractive for transportation and distributed generation applications, which may see the majority of their operating hours at low load.

The overall electrical efficiency, η_{el}, is defined as the ratio of the net power provided by the system, $\dot{W}_{sys}$ (W) to the flow rate of chemical energy into the system:

$$\eta_{el} = \frac{\dot{W}_{sys}}{\dot{m} HV} = \eta_{BOP} \times \eta_V \times \eta_{ideal} \tag{9.6}$$

where the BOP efficiency, η_{BOP}, reflects the efficiency of the BOP components at converting $\dot{W}_{fc}$ to net power:

$$\eta_{BOP} = \frac{\dot{W}_{sys}}{\dot{W}_{fc}} \tag{9.7}$$

The overall electrical efficiency can vary through a wide range depending on the fuel type and application.

Figure 9.5 illustrates the relationship between fuel cell efficiency metrics and depicts representative efficiency behavior for both hydrogen-fueled systems and natural gas-fueled systems. For the hydrogen-fueled PEMFC, efficiency decreases

[3]In the case of direct methanol fuel cells, for which fuel crossover is significant, and for fuel cells operating with more complex fuels, the description of the fuel cell efficiency requires additional considerations.

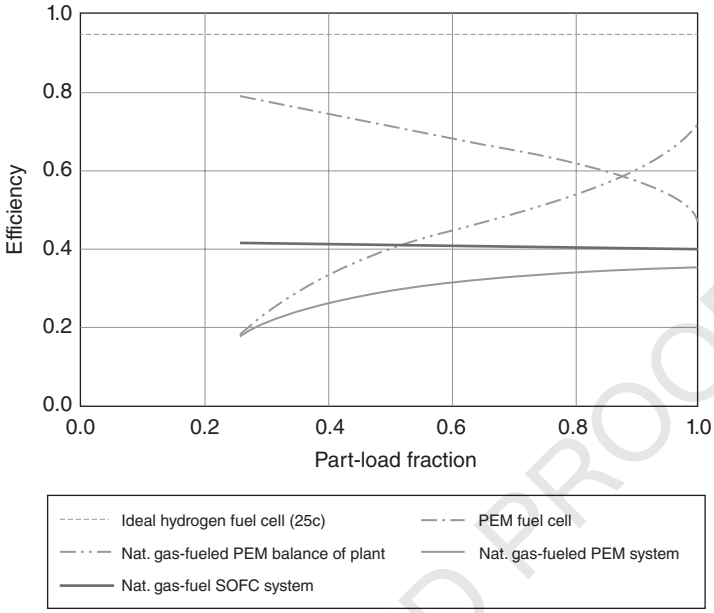

Figure 9.5 Fuel cell efficiency metrics varying with load fraction and system type. Representative trends are shown here, but actual performance varies widely with system design. (*See electronic version for color representation of this figure.*)

with increasing load fraction. However, the efficiency of the BOP increases with increasing load fraction as thermal losses from the fuel processor become relatively less important. As an example, the net effect for a residential natural gas-fueled PEMFC system is a relatively flat efficiency curve down to about 50% load, followed by a steep decrease at lower loads. The residential natural gas-fueled SOFC system tends to have a flatter profile throughout the performance range due to simplified fuel processing requirements. Ellamla et al. provide a more detailed discussion of part load performance for residential cogeneration systems [53].

9.4.2 Dynamic Operation

Fuel cell dynamic operation reflects three different phenomena that occur at different rates: (1) the electrochemical reaction, which responds very quickly; (2) the mass transport processes within the stack, which respond more slowly; and (3) the response of the system equipment, which is likely to be even slower. Within the electrode, the electrochemical reaction forms a charge double-layer across the interface between the electrically conductive phase and the ion-conducting phase, which behaves like a capacitor. This double-layer forms in parallel to the charge transfer pathway, leading to the simplest electrical description of the fuel cell, the Randles circuit illustrated in Figure 9.6a.

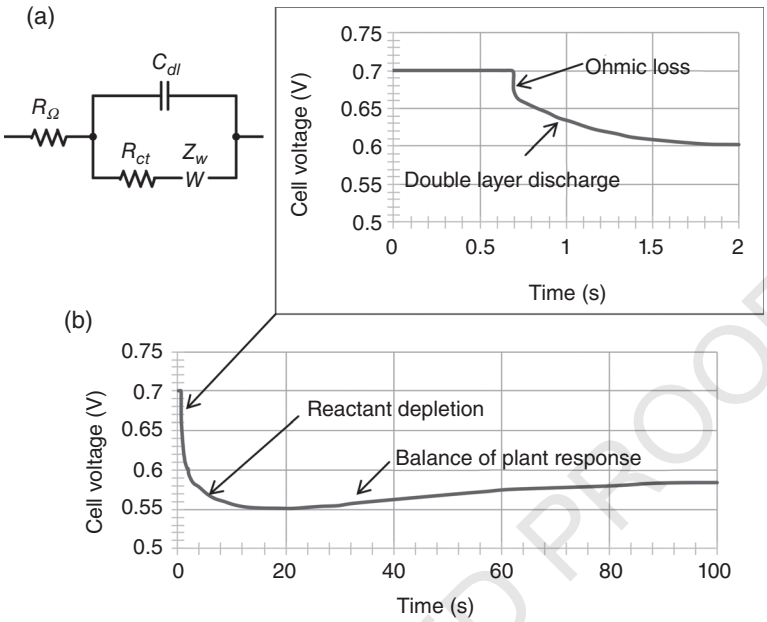

Figure 9.6 Dynamic fuel cell circuit model: (a) dynamic response at short times described by the Randles circuit; (b) over a longer time period, the response is characterized by multiple timescales.

In the Randles circuit, the charge transfer pathway is characterized by a charge transfer resistance, R_{ct}, and an additional mass transfer impedance, which may behave like a simple resistor or a more complicated nonlinear Warburg impedance, Z_W. The final element in the circuit is a resistive element, R_Ω, which reflects the losses associated with electrical and ionic conduction through the cell. The cell surface area for the double-layer is formed in the microporous electrode and is quite large, leading to a very large capacitance, C_{dl}. On the other hand, the large surface area for the reaction results in a small charge transfer resistance, R_{ct}. The time constant for the resulting resistor-capacitor (RC) circuit is generally small (less than 1 s for PEM fuel cells). In contrast, the mass transport processes in the cell involve depletion or accumulation of chemical species in the electrode pores and flow channels due to the fuel cell reactions, and occur at somewhat longer time constants. Finally, the fuel and oxidant supply systems and cell temperatures respond at even slower rates (of the order of 10–100 s for a typical PEM fuel cell) [54].

Figure 9.6b illustrates the typical response of a fuel cell to a step increase in the applied current. Initially, the voltage drops instantaneously due to the ohmic resistance of the cell. The voltage then gradually declines further to a new quasi-steady value over a timescale determined by the electrochemical processes characterized by the Randles circuit (~1 s). However, the new, higher cell current will begin depleting the concentration of reactants in the flow channels, leading the cell

voltage to continue to decline. Finally, the system will respond over a longer time-scale by increasing the air compressor flow, adjusting the hydrogen supply valve (or increasing the flow through the fuel processor), and responding to the changing thermal characteristics of the stack, thus bringing the system to a new steady condition. A step decrease in current results in the opposite series of changes. Several dynamic analyses of these processes can be found in the literature with models implemented using tools commonly employed for electrical system analysis [54–57].

The actual response of a fuel cell system depends heavily on the BOP design. If the BOP, especially the compressor, responds quickly enough, the time constant can be significantly reduced. Figure 9.7 plots the experimental time-domain response of a 1.2 kW PEM fuel cell stack that has been accelerated with a compressor over a 6-second test period [21]. Initially under no-load conditions, the fuel cell stack voltage v_{FC} stays at 43 V. With a step increase in resistive loading, the voltage presents an undershoot determined by the double-layer discharge and the local reactant depletion, but then returns to an equilibrium condition of 27.2 V. The compressor reacts immediately after the load step, thus limiting the dynamic time constant to a small value. At the 5.4 s time mark, following the instantaneous load removal, the voltage returns to the open-circuit voltage condition without overshoot, but the power presents an overshoot due to the delayed response of the BOP.

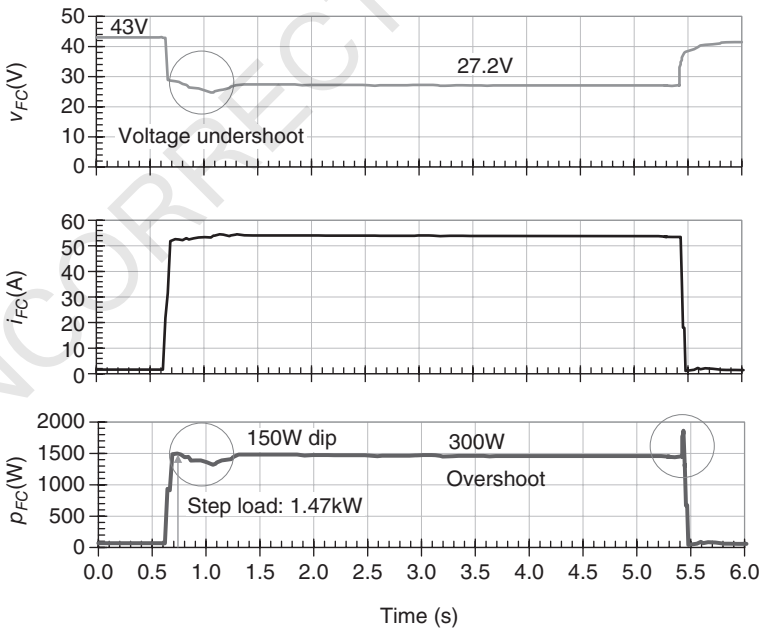

Figure 9.7 Experimental waveforms of a 1.2 kW PEM fuel cell stack under step-up and step-down load change conditions.

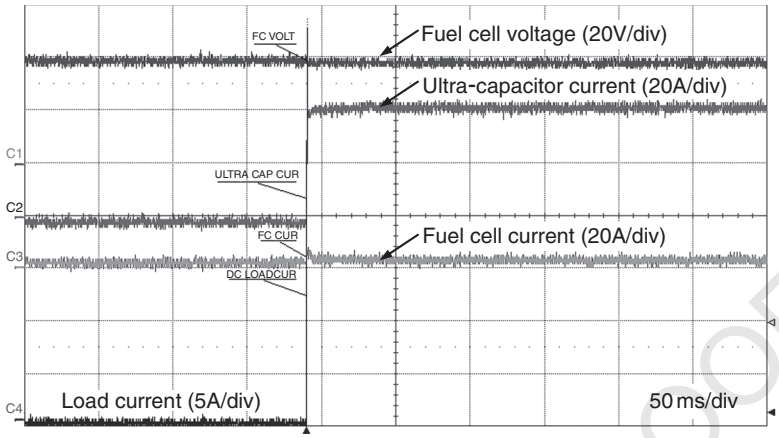

Figure 9.8 Fuel cell dynamic load step responses with added 145 μF ultracapacitor.

9.4.3 Dynamic Operation with a Paralleled Ultracapacitor

Referring to Figure 9.7 for a load step with no externally added capacitance, the fuel cell voltage shows a noticeable dip under the load step condition. As suggested by the literature [58], it is possible to reduce such a voltage dip with a large capacitor bank or ultracapacitors. Figure 9.8 demonstrates a test case with an added 145 μF ultracapacitor. With a step load of 40 A, the ultracapacitor absorbs nearly all the load current, and the fuel cell current and voltage remain near constant. If the plot were observed over a much longer time period, the capacitor current would return to zero, and the fuel cell current would equal the load current. This test result indicates that an ultracapacitor stabilizes the fuel cell voltage and current during load dynamics and is a good companion for the fuel cell stack.

9.5 FUEL CELL POWER SYSTEM ARCHITECTURE

A complete fuel cell power system requires a BOP to manage the power output and to ensure the fuel cell operates under the most efficient and reliable conditions. In addition, a power electronics system is needed to regulate the output of the fuel cell under different load conditions and to convert the output to different power formats.

9.5.1 Balance-of-Plant

A typical fuel cell power system is shown in Figure 9.9. The core of the entire fuel cell power system is the fuel cell stack, which consists of tens or even hundreds of cells connected in series. As discussed in conjunction with Figure 9.1, the BOP controls flow rate, pressure, temperature and humidity using heat exchangers,

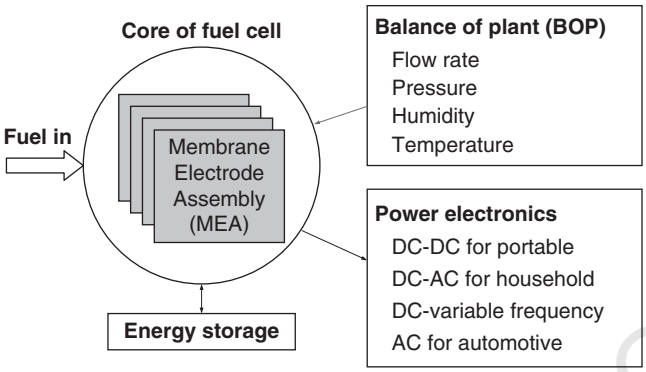

Figure 9.9 Fuel cell system architecture showing the stack as the core, BOP, and power electronics blocks.

humidifiers, compressors and blowers. The significance of the BOP controls can be illustrated by the 80 kW transportation PEM fuel cell system described in the US DOE's MYRDDP [8]. The BOP for this application incorporates a compressor and expander to control the stack pressure and pumps to supply water for cooling and humidification, and recovers the power from the exhaust air. The state-of-the-art system requires 11 kW with the expander and 17.3 kW without the expander for the air compression system. A multi-year research plan has been undertaken to reduce such ancillary power to 8 and 14 kW with and without the expander. However, even with these improvements, maintaining the pressure and humidity of the stack reactants to support efficient cell operation will still require an additional 10–18% of the stack net power. While other approaches have been explored to control PEM hydration, such as periodically driving individual cell currents to high rates to internally generate water for hydration [59], operating the stack at pressure with humidification remains the favored mode of control despite the ancillary power burden.

9.5.2 Fuel Cell DC Power Systems

In addition to controlling the BOP, the power management system must provide stable voltage for the associated load. To stabilize the output voltage and to limit the effect of voltage fluctuations imposed by the load on the fuel cell, a large capacitor bank can be added across the fuel cell output, but the life expectancy of such a capacitor bank can be a concern, especially with the use of electrolytic capacitors. As shown in Figure 9.10a, it is possible to add a DC-DC boost converter for each fuel cell and connect the converter outputs in series, which not only stabilizes the load-side voltage, but also helps voltage balancing and provides the boost function [60]. However, the cost is proportionately increased as the number of cells increases. Therefore, instead of adding DC-DC converters at the cell level, most high-voltage systems adopt a DC-DC converter as the buffer stage in between the load and the fuel cell stack, as shown in Figure 9.10b [61–65]. In large fuel cell systems, [66–68]

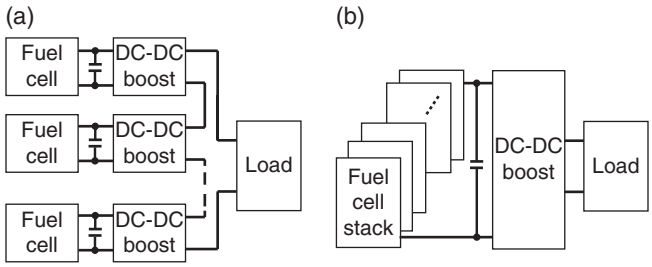

Figure 9.10 Fuel cell output with rch fuel cell and stack the boost converter output; (b) adding a boost converter for the entire series connected stack.

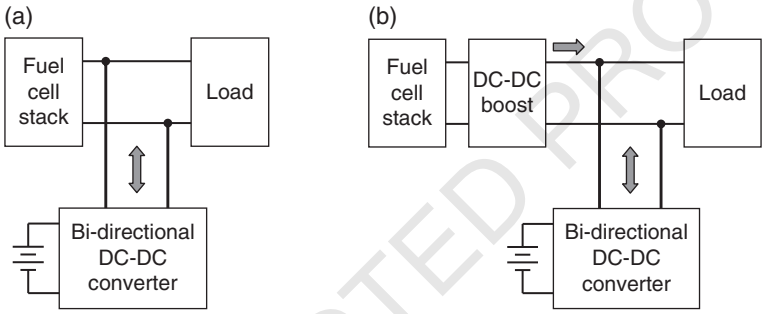

Figure 9.11 Fuel cell systems with added battery energy management: (a) matching fuel cell stack output voltage with load, but adding a bi-directional DC-DC converter for the battery; (b) adding a uni-directional DC-DC boost converter for the fuel cell and a bi-directional DC-DC converter for the battery.

suggest the entire stack be split into multiple substacks connected in series, with each substack incorporating an isolated DC-DC converter with inputs connected to each substack and outputs connected in series to provide high-voltage DC output.

For a fuel cell system with multiple sources, especially with an added battery pack to help stabilize the fuel cell output voltage, additional power management converters are needed. In electric vehicles where cost is very sensitive, the fuel cell is normally stacked at a higher voltage level that can directly power the load, with an added battery-powered DC-DC converter that must be bi-directional as shown in Figure 9.11a and Figure 9.11b [65, 69–74]. Depending on system requirements, the added battery and associated bi-directional DC-DC converter can be used as an energy buffer to serve as power management for a stack with a significantly lower power rating for cost reduction.

In [73] a battery coupled with a bi-directional DC-DC converter was proposed to serve multiple purposes for fuel cell electric vehicles. Basic functions of the bi-directional DC-DC converter are described as follows.

1. During start-up, a low-voltage 12V battery charges the high-voltage 300V DC bus to provide sufficient bus voltage to power the fuel cell's ancillary systems, especially the air compressor. The battery is under "discharging mode."
2. After fuel cell power is established and during vehicle regenerative braking, the high-side DC bus voltage recharges the battery, and the battery is under "charging mode."
3. During vehicle accelerating and uphill driving conditions, the battery supplements the power to the high-side DC bus, and the battery is under "discharging mode."

With a large difference in voltage scale between input and output, the DC-DC converter circuit in [73] adopts an isolation transformer that changes the voltage ratio to allow switching devices rated according to their respected voltage levels. In [74], however, with a similar system architecture and similar voltage scale between battery and fuel cell, non-isolated circuit topologies are adopted. In addition, the system in [74] has a load voltage much higher than that of the fuel cell and battery, so two converters for both fuel cell and battery are needed to match the DC bus voltage, as shown in Figure 9.11b.

9.5.3 Grounding Requirement for Fuel Cell AC Power Systems

For a power electronic circuit, the selection of circuit topology with or without isolation typically depends on cost and efficiency considerations. If the input and output voltage ratio is high, using transformer isolation is naturally the choice because it allows the semiconductor devices to be sized according to the voltage and current levels. If the input and output voltage levels are similar, non-isolated circuit topologies are normally adopted to reduce the cost and increase the efficiency.

In some special power conversion cases, isolation is required by regulations. For example, when a fuel cell system includes both AC and DC power outputs, the National Electric Code Article 692 (NEC-692) requires that the DC ground be bonded to the AC grounding system [75]. The requirement that DC and AC share the same ground implies that the fuel cell DC output must be isolated from the AC lines. As most fuel cell output DC is low voltage relative to the AC line voltage, the isolation can be implemented with an isolated DC-DC converter which naturally provides isolation and voltage boost through a high-frequency transformer.

Figure 9.12 indicates the grounding configuration of a fuel cell power system that consists of a DC voltage at the fuel cell output V_{dc} and an AC voltage at the inverter output V_{ac}. The fuel cell is represented by a fixed DC source V_{fc} along with an internal nonlinear resistance R_{fc}. The negative terminal of V_{fc} and the neutral of the AC lines are connected to the same ground node. Thus, the power electronics circuit requires isolation to avoid a short-circuit between input and output. For a photovoltaic (PV) power system, such a source grounding is not required by NEC (NEC-690) [75] because the PV panel does not have an associated BOP control system, and thus the circuit isolation is unnecessary in PV power systems.

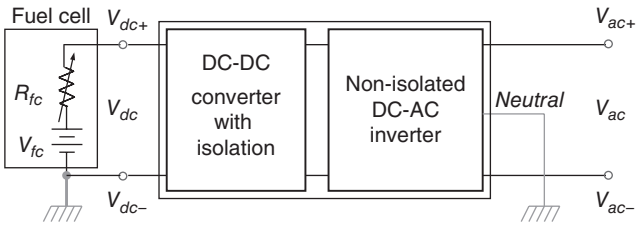

Figure 9.12 Grounding system requirement for a fuel cell AC power system.

9.6 POWER ELECTRONICS FOR FUEL CELL APPLICATIONS

A power electronic circuit contains mainly switching devices and passive components to convert the input and output with different magnitudes or different formats such as DC or AC. For fuel cell applications, the input source is DC, so the major components are DC-DC converters and DC-AC inverters.

9.6.1 DC-DC Converters

Basic DC-DC converter topologies can be categorized into buck (or step-down), boost (or step-up), and buck-boost [76–78]. Without isolation, these basic DC-DC converters are more suitable for similar voltage levels between input and output to avoid a significant penalty on switching device voltage and current ratings. With isolation, the topology choices are numerous, but the selection process is non-trivial. In general, most fuel cell stacks operate at a relatively low voltage. To obtain a high-voltage AC output, the fuel cell output voltage must be boosted with a high conversion ratio to a level that is higher than the peak value of the AC output voltage. In this case, an isolated DC-DC circuit with a high voltage conversion function is the natural choice.

Single-Switch Isolated DC-DC Converters

The three basic non-isolated DC-DC converter topologies can be extended to isolated buck (or forward), isolated boost, and isolated buck-boost (or flyback) converters [76–78]. These simple isolated DC-DC converters require only one switching device, but their transformers typically operate in the first quadrant where both flux density and magnetic field strength are positive. In other words, the magnetic core is not fully utilized with single-switch type converter circuits.

Although single-switch type DC-DC converters serving as the boost and buffer stage between source and inverter are not widely adopted in fuel cell applications, other low-power renewable energy sources, especially PVs, tend to prefer single-switch type converters at the low-power panel or subpanel level because of the cost and parts-count considerations. Several variations of single-switch type DC-DC converters are available to convert low voltage to high voltages. In [79–88],

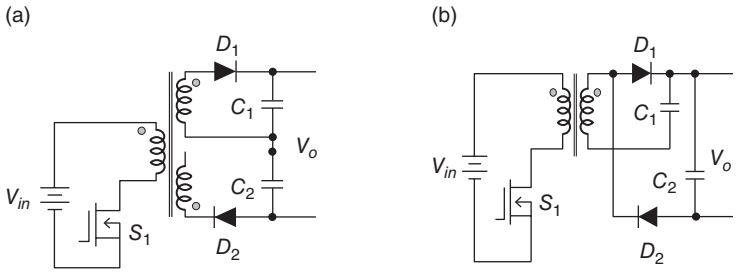

Figure 9.13 Single-switch forward-flyback DC-DC converters suitable for low-cost and low-power applications: (a) with one switch and two secondary stages connected in series; (b) a shared winding type with one switch and two secondary stages that share the same winding.

high-voltage boost ratio power conversions were proposed using the combination of boost and flyback converters. These topologies are mainly non-isolated and are more suitable for PV applications because the NEC does not require the PV output terminal to be grounded.

Shown in Figure 9.13, two isolated DC-DC converters employ the combination of forward and flyback converters using only one switch [89–94]. The energy transfer with such a combination can be performed during switch turn-on and turn-off periods, thus achieving better transformer utilization and overall efficiency. These converters can be used for fuel cells where isolation is required, but are limited to relatively low-power applications due to high switch stresses.

The converter circuit shown in Figure 9.13a is considered a hybrid forward-flyback DC-DC converter that employs only one switch and two secondary stages connected in series. When switch S_1 is turned on, the forward converter transfers the energy to output capacitor C_1 through diode D_1 and the top-side secondary winding. When switch S_1 is turned off, the flyback converter transfers the energy to output capacitor C_2 through diode D_2 and the bottom-side secondary winding. For Figure 9.13b, a hybrid forward-flyback DC-DC converter employs only one switch and one shared secondary winding to reduce the component counts. In [89], an active clamping switch was added, and an operating mode was proposed to turn on the switch under constant on-time that turns on and off the switch under zero voltage and near-zero current condition. The hybrid structure also allows the transformer flux to swing in both first and third quadrants and fully utilizes the magnetic core. With near-zero switching loss and full utilization of the magnetic core, the power conversion efficiency is substantially higher than the conventional forward or flyback converter alone. The reported converter peak efficiency in [89] is 97.5% under low-voltage 45 V input and high-voltage 400 V output condition for a 250 W system.

Multiswitch Isolated DC-DC Converters

Although the single-switch versions of the DC-DC converters can fully utilize the magnetic core and achieve satisfactory power conversion efficiency, the switch current stress can be excessively high for high-power systems. It is necessary to add

switches to share the duty among them and to reduce the stress of the individual switches. As an alternative, the two basic two-switch isolated DC-DC converters are push-pull and half-bridge converters [76–78]. The push-pull converter utilizes the center-tap transformer, with the center of the winding connecting to the source and the two ends of the winding connecting to switches that turn on and off complementary to one another. Thus, the transformer flux swings between positive and negative symmetrically, which allows full utilization of the magnetic core. The main issue with this topology is the voltage stress of the individual switch, which sees twice the input voltage, thus requiring power semiconductor devices with higher voltage ratings. The half-bridge converter utilizes split capacitors to provide two voltages that are half the input voltage. The main issue with this topology is the switch current stress, which is essentially double because the voltage supplied to the transformer is half.

For high power applications, the voltage and current stresses must be within the specified operating range for the switch, and thus the most popular circuit is the full-bridge converter [76–78]. The full-bridge can be considered as two half-bridge converters that connect the transformer winding in between two phase-leg outputs. Instead of using the middle point of the capacitor or the center tap of the transformer winding as one of the primary nodes, which tends to be unbalanced with component mismatch, the full-bridge converter offers relatively balanced voltage between positive and negative cycles. The voltage stress is the same as the fuel cell input supply, and the current stress is the same as the rated input current.

Based on the switching circuit input, all multiswitch DC-DC converters can be configured with voltage source or current source. If the input of the switching circuit is fed by a stiff voltage source, typically a capacitor, then the circuit is considered a voltage-source or voltage-fed converter. If the switching circuit is fed by a stiff current source, typically an inductor, then the circuit is considered a current source or current fed converter. The abovementioned push-pull, half-bridge, and full-bridge converters can each be configured for operating with a voltage or current source. If the primary-side switching circuit is a voltage source, then the secondary-side rectifying circuit output must be connected to the output capacitor through an inductor. In other words, a voltage source input must be buffered with a current source secondary before supplying the output. For current source converters, the primary-side switching circuit is fed with a stiff current source or a large inductor, and the secondary-side rectifying circuit output can be directly connected to the output capacitor.

The converter switching devices are normally switching at high frequencies, tens of kilohertz (kHz) for high-power systems and hundreds of kHz for low-power systems, and the current slew rate (i.e., di/dt) is quite high such that it tends to produce a high voltage spike. Additionally, the turns-ratio of the transformer needs to be high enough to accommodate the fuel cell input voltage variation, which typically drops 50% from no load to full load following the polarization curve. For voltage source converters, under light-load condition, the transformer secondary output voltage is more than 50% higher than the output voltage. Similarly, for

current source converters, the transformer primary-side input voltage is more than 50% higher than the source voltage. Since the output side of the converter is a rectifier circuit, for a voltage source converter, the output diodes must be rated at a higher voltage. For current source converters, however, with overvoltage on the primary side, the switches must be rated at a higher voltage. To reduce the voltage stress, a clamping circuit is normally added to reduce the stress on diodes in voltage source converters and on switches in current source converters. The clamping circuit can be passive or active. With active clamp, since the clamping switches are turned on and off under zero-voltage and zero-current conditions, and the energy is circulating between capacitors, the efficiency is generally higher [73, 95, 96]. However, the addition of the clamping switch and associated control tends to increase the cost and complexity.

To explain the difference between voltage and current source converters, a full-bridge converter is used as the example. Figure 9.14a and Figure 9.14b compare the active clamp circuit arrangements between voltage source and current source converters. In Figure 9.14a, the primary-side full-bridge switching circuit consists of four switches, S_1–S_4, and is fed by a voltage source V_{in}, which connects across the fuel cell output with a relatively large capacitor C_{in} across the converter

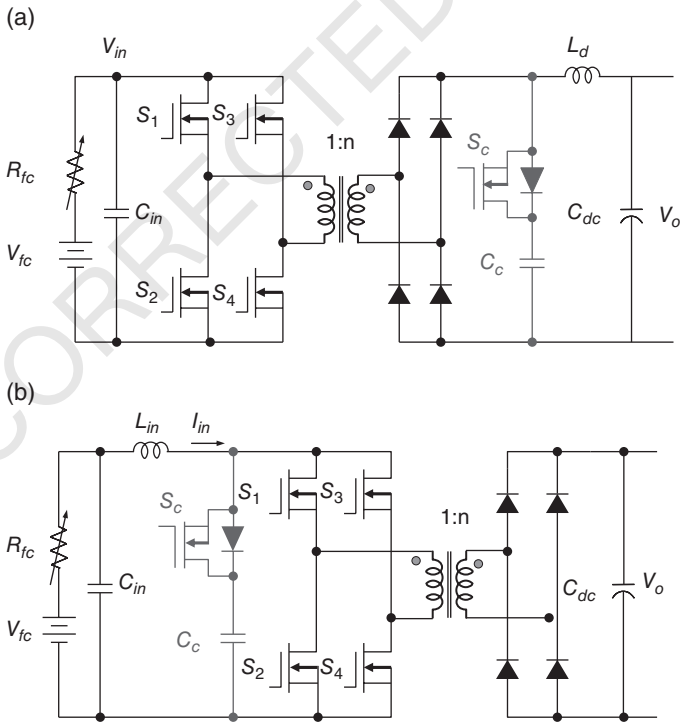

Figure 9.14 Two different full-bridge DC-DC converters: (a) voltage source converter with active clamp; (b) current source converter with active clamp.

input. The secondary rectifier diode circuit feeds through a current source buffer inductor L_d to the DC output capacitor C_{dc}. The rectifier output voltage is the input voltage times the turns ratio, n, plus the leakage inductance and di/dt induced voltage, and thus is much higher than the output voltage V_o, especially under light-load conditions. Therefore, an active clamp circuit that consists of clamping switch S_c and clamping capacitor C_c is added to reduce the voltage stress of the rectifier diode.

In Figure 9.14b, the primary-side full-bridge switching circuit is fed with a large-size inductor L_{in} which represents a stiff current source I_{in}. The secondary rectifier diode circuit feeds directly to the output capacitor C_{dc}. The transformer primary voltage is the output voltage divided by the turns ratio, n. The switches see a voltage that is the sum of the transformer primary voltage and the leakage inductance-induced voltage, and is much higher than the input voltage V_{in}. Therefore, an active clamp circuit that consists of clamping switch S_c and clamping capacitor C_c is added between the inductor and the switching circuit to reduce the voltage stress of the switches S_1–S_4.

Soft-switching DC-DC Converters with Isolation

The full-bridge converter can operate under pulse width modulation (PWM) duty cycle control or phase-shift modulation (PSM) conditions. With PSM, the converter can achieve zero-voltage switching (ZVS) [97, 98]. The problems with the PSM scheme are loss of ZVS at light loads, and circulating currents between the winding and switches when either two upper switches or two lower switches are turned on simultaneously. When ZVS is not achieved, the switching loss is high, and during current circulating periods, the conduction loss is high. Therefore, many remedy circuits have been proposed to improve the efficiency of phase-shift modulated converters [99, 100].

Figure 9.15 depicts a hybrid-switching type soft-switching DC-DC converter that is of particular interest. This circuit employs a hybrid switching concept similar

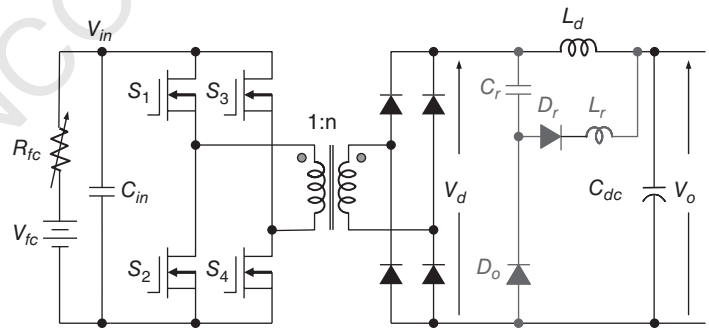

Figure 9.15 A hybrid soft-switching DC-DC converter combining a conventional full-bridge voltage source PWM converter and a resonant circuit in the secondary side for soft-switching operation.

to the idea described in [101–103]. The basic hybrid switching idea combines conventional PWM with resonant operations. The original full-bridge converter consists of switches S_1–S_4, a transformer, a rectifier bridge, inductor L_d, and output capacitor C_{dc} that operate in traditional PWM mode. The added components consist of output freewheeling diode D_o, resonant capacitor C_r, resonant inductor L_r, and resonant branch diode D_r. There are two operating periods: (a) PWM duty cycle on-period in which the diode bridge output voltage is the input voltage times the turns ratio, or $V_d = n \cdot V_{in}$; and (b) PWM duty cycle off-period in which the diode bridge output voltage is zero, or $V_d = 0$.

When $V_d = n \cdot V_{in}$, the conventional PWM current i_L goes through L_d and charges C_{dc}. The resonant current i_r is created through C_r, L_r, and resonant branch diode D_r. Resonant components L_r and C_r can be designed such that i_r resonates to zero before or at the end of PWM duty, so diode D_r is always zero-current turn-on and turn-off. The buffer inductor L_d is a large inductor compared with L_r, and maintains continuous current i_L during both PWM on and off periods. When one of the primary-side switches is turned off, the transformer primary current, i_L/n, is sufficient to discharge the switch output capacitance that creates a zero-voltage turn-on for the switch. When $V_d = 0$, the PWM current i_L continues freewheeling through D_o, C_r, and L_d. Therefore, the primary side no longer sees circulating current.

If the input voltage is high during light load conditions, the resonant period may exceed the PWM duty, which will result in non-zero current turn-off for diode D_o, which deteriorates the efficiency. In this case, the variable frequency approach can be applied to improve the light-load efficiency. The concern with the variable frequency approach is the electromagnetic interference (EMI) frequency spectrum. However, if variable frequency operation is not objectionable in some particular applications, the variable frequency type, resonant type DC-DC converter is an alternative to a more PWM-oriented converter. Figure 9.16 depicts a popular resonant DC-DC converter that utilizes the magnetizing current i_M to discharge the primary-side switches to achieve zero-voltage turn-on. The resonant current i_r swings to zero before or at the switch turn-off, thus achieving zero-current switching for both primary-side switches and secondary-side diodes [104–108].

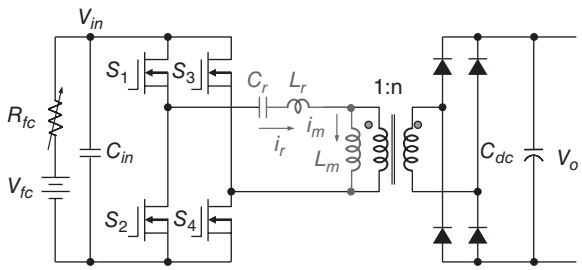

Figure 9.16 Resonant DC-DC converter showing the circuit structure where L_r can be externally added or part of the leakage inductance of the transformer.

Multiphase DC-DC Converters with Isolation

For stationary power system applications, if the fuel cell output voltage is below 50 V, but the power requirement is 5 kW and above, then the single full-bridge DC-DC converter may experience a large current stress. Although it is possible to parallel switches, the parasitic components can result in unnecessary losses. A multiphase DC-DC converter using parallel multiple-leg converters can be employed for high-power applications while avoiding parasitic component losses. The individual leg can be a half-bridge, full-bridge, or resonant type [62, 109–113].

To reduce the current stress to a level that discrete semiconductor devices can handle, the number of phases needs to be as high as possible. Figure 9.17 shows a three-phase, six-leg DC-DC converter example for low-voltage fuel cell applications in [62, 109–111]. Analogous to the car engine in the automotive industry, where the high horsepower engine evolved from a single cylinder to multiple cylinders such as the V6 engine to improve the fuel efficiency and smooth the torque output, this circuit topology was named the "V6" converter. The three phases are grouped into different blocks including switches S_{11}–S_{14} as the first block, switches S_{21}–S_{24} as the second block, and switches S_{31}–S_{34} as the third block. Each block forms a full-bridge converter. The secondary transformer windings are connected in Y configuration so the line-to-line output voltage is twice the supply voltage times the turns ratio. For example, the maximum voltage between a and b, or v_{ab}, equals $2{\cdot}n{\cdot}V_{in}$. In other words, under full duty condition, $V_o = 2{\cdot}n{\cdot}V_{in}$. This double voltage conversion ratio allows a smaller turns ratio, which will help reduce the leakage inductance. As the three phases operate 120° apart in one switching cycle, the effective switching frequency is three times, and thus the size of the buffer stage inductor L_d can be largely reduced. When each phase-conducting duty cycle is 120° or higher, the voltage conversion ratio is fixed at the maximum, but three outputs are no longer interrupted, which means the output current is ripple-free.

All PWM, PSM, and LLC soft-switching circuits can be applied to each full-bridge converter. For low-voltage fuel cell converters, the semiconductor devices

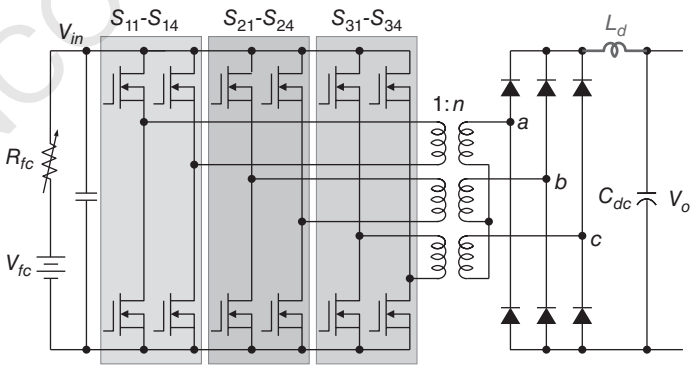

Figure 9.17 A three-phase, six-leg (V6) DC-DC converter suitable for high-power but low-voltage fuel cells.

can achieve zero-voltage switching even with low transformer leakage inductance because the energy needed to discharge the device output capacitance is relatively low. Hence, overall this V6 converter is quite suitable for low-voltage, high-power fuel cells with key features like (1) high-efficiency power conversion because of soft switching, (2) small passive components because of the ripple cancellation with interleaved operation, and (3) reduced transformer leakage inductance and its related loss.

9.6.2 DC-AC Inverter

Basic DC-AC inverter circuits and their modulation methods can be found in textbooks [76, 77, 114–116]. Figure 9.18 shows two example circuit diagrams: (a) a full-bridge single-phase inverter and (b) a three-phase bridge inverter. For the same inverter circuit, different modulation methods can significantly affect the efficiency, waveform quality, and filter design. Considering a single-phase full-bridge inverter, bipolar and unipolar sinusoidal pulse width modulations (SPWMs) are two major modulation methods. For three-phase inverters, with the absence of multiples of three times harmonic currents, different SPWM approaches with and without neutral signal injection for the reference signals can be used to increase the DC bus voltage utilization [116].

A single-phase full-bridge inverter example is illustrated in Figure 9.18a. The inverter comprises two phase legs: phase-leg-a consisting of Q_1 and Q_2 with output node a, and phase-leg-b consisting of Q_3 and Q_4 with output node b.

Figure 9.19 illustrates the basic SPWM method, which is to compare a sinusoidal reference voltage and a carrier signal v_c. For phase-leg-a, the reference voltage signal is $v_{ref\text{-}a}$. Between node-a and negative DC bus node-0, the modulated phase output node-a voltage, v_{a0}, swings from V_{dc} to 0 or 0 to V_{dc} with a pulse width corresponding to the comparison results. If phase-leg-b switches complementarily, the output node-b v_{b0} voltage will be complementary to v_{a0}. In other words, when v_{a0} is V_{dc}, v_{b0} will be 0, and when v_{a0} is 0, v_{b0} is V_{dc}. The overall inverter output voltage across a and b, $v_{ab} = v_{a0} - v_{b0}$ will then swing between $-V_{dc}$ and $+V_{dc}$. This voltage can be defined as the differential mode (DM) voltage in electromagnetic

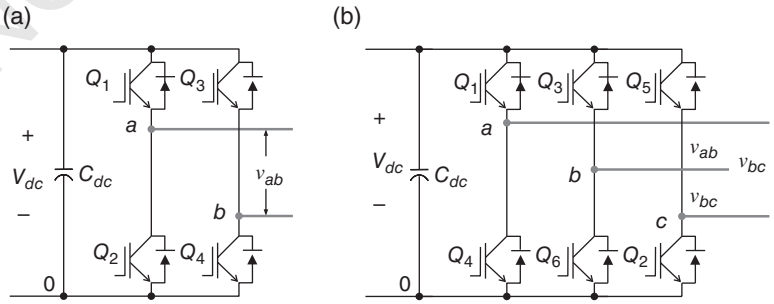

Figure 9.18 Circuit diagrams of typical inverters: (a) single-phase; and (b) three-phase.

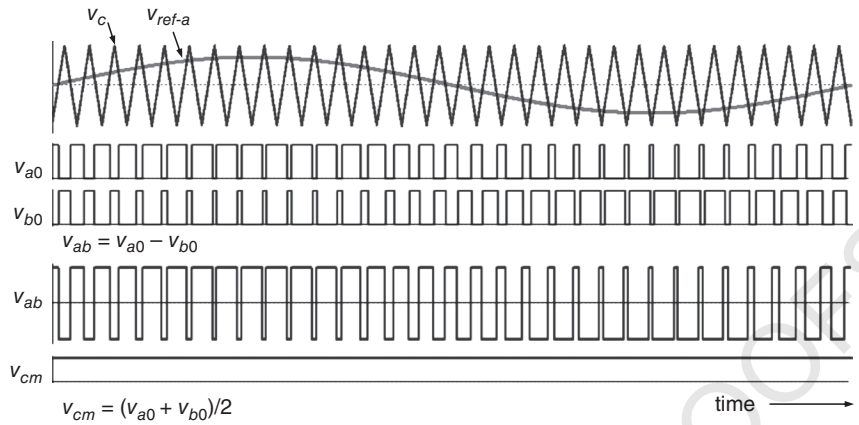

Figure 9.19 Bipolar SPWM differential and common mode output waveforms.

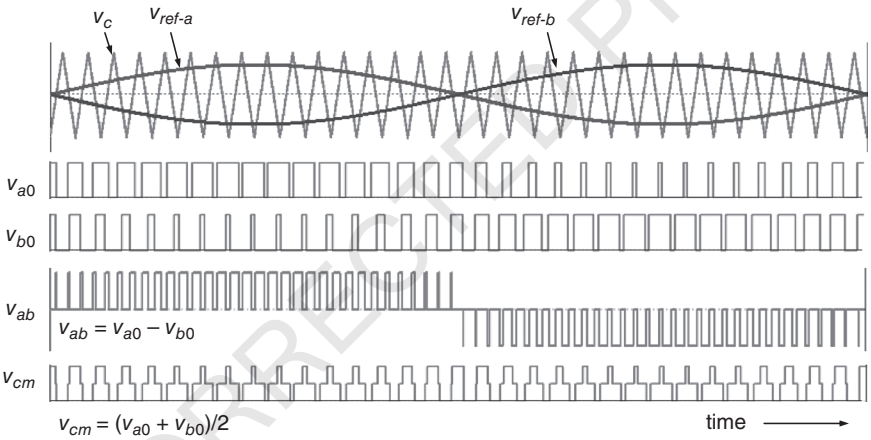

Figure 9.20 Unipolar SPWM differential and common mode output waveforms.

interference (EMI) studies. To the overall EMI, it is also important to pay attention to the common mode (CM) voltage, which can be defined as $v_{cm} = (v_{a0} + v_{b0})/2$. As indicated in Figure 9.19, with bipolar modulation that has complementary output voltages v_{a0} and v_{b0}, the common mode voltage is a constant with the value of $V_{dc}/2$. As the DC output does not emit high-frequency noise, this bipolar SPWM allows the CM EMI filter to be minimized. However, its DM output harmonics are excessively high because it swings between $-V_{dc}$ and $+V_{dc}$.

To reduce the output harmonics and high-frequency noise, unipolar SPWM is normally adopted. Figure 9.20 illustrates an option for unipolar SPWM operation. In this case, individual legs are modulated with an independent SPWM. For phase-leg-a, the reference signal is $v_{ref\text{-}a}$, and for phase-leg-b, the reference signal is $v_{ref\text{-}b}$. The DM output $v_{ab} = v_{a0} - v_{b0}$ swings between $+V_{dc}$ and 0 in the positive line cycle,

and between 0 and $-V_{dc}$ in the negative line cycle. In either positive or negative line cycle, the voltage swings in one direction only, thus this modulation is called unipolar modulation. Its harmonic contents are significantly lower because the equivalent switching is doubled, and the most significant frequency is around twice the switching frequency, which allows much smaller size harmonic filters and DM EMI filter. The CM voltage ($v_{cm} = (v_{a0} + v_{b0})/2$), however, presents high-frequency components that swing between $+V_{dc}$ and 0. This implies that the CM EMI filter must be much larger than the one used in the bipolar modulation method.

For compliance purposes, the complete single-phase inverter should include the abovementioned bridge-type inverter, a harmonic filter, a DM EMI filter, and a CM EMI filter. Figure 9.21 depicts the arrangement of a complete inverter system that consists of a full-bridge inverter. The common mode current path consists of a parasitic capacitance between the switching nodes and the ground through heat sink and the CM EMI filter. If the switching frequency is high enough, the harmonic filter and EMI filter may be combined in one. The CM filter, however, is not avoidable due to parasitic components and high-speed switching of the devices. A CM filter contains a CM inductor L_{cm}, which blocks the current from the inverter to the load, and two CM capacitors C_{cm1} and C_{cm2} which conduct the CM current through the ground loop. Design of an inverter requires a comprehensive understanding of the impact of the modulation method, switching frequency, switching speed, parasitic components, and filter design.

In practice, the size of passive components, including all the filter capacitors and inductors and heat sink, will dominate the entire inverter size and weight. Filter component size and associated costs can be reduced by increasing the switching frequency. Soft-switching that allows the inverter to switch at a higher frequency while maintaining high efficiency is attractive for stationary fuel cell applications [117–134]. High-efficiency design can also reduce the size of the heat sink and associated cost. Among different soft-switching inverters, the auxiliary resonant snubber approaches, which have been reported to exhibit greater than 99% efficiency using silicon devices [130, 131], are quite suitable for medium-power applications.

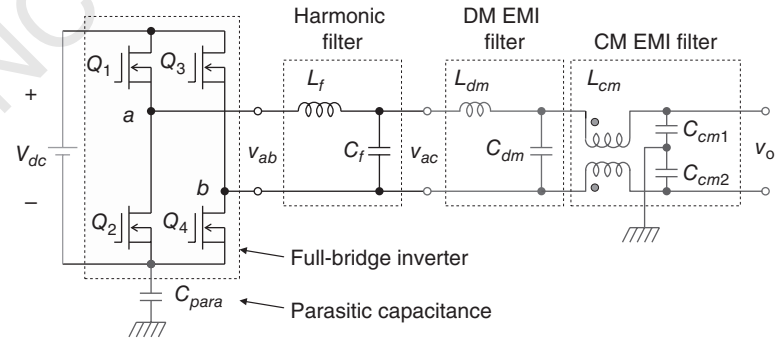

Figure 9.21 A complete inverter circuit with all filters added.

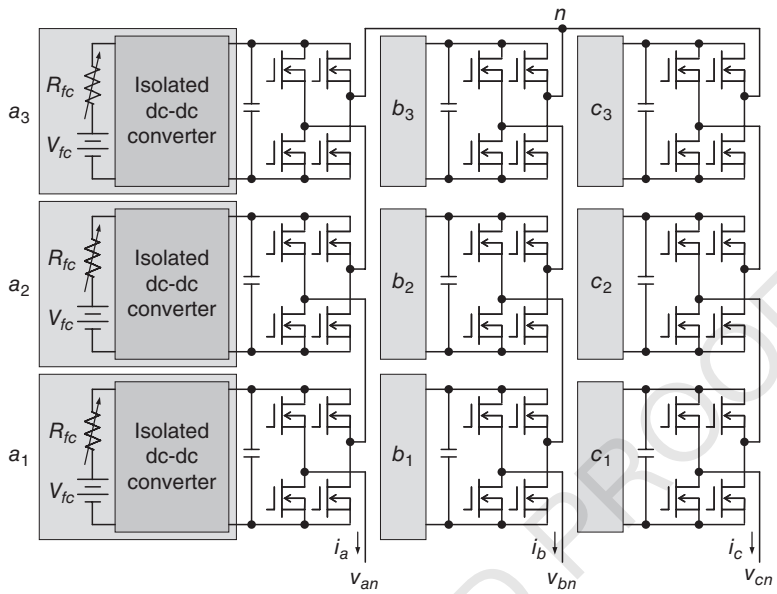

Figure 9.22 Cascaded multilevel inverter configuration for large-scale fuel cell systems.

For megawatt (MW)-scale systems, multilevel inverters are necessary to reduce the voltage and current stresses on switching devices and to reduce the size and weight of passive components [135–142]. Since the fuel cell stack must be grounded, multilevel inverters must have isolated DC-DC converters between the stack and the inverters. Figure 9.22 depicts a cascaded multilevel inverter (CMI) for high-voltage, high-power fuel cell power conversion systems. The number of levels can be chosen as many as needed for the application. In this example, three fuel cell stacks per phase are configured as a single unit that produces a PWM inverter output with a relatively low switching frequency AC. All AC outputs of each phase are connected in series with interleaved operation. With a small output filtering circuit, the current can be a clean sinusoidal, as shown in the simulation results of Figure 9.23. The only design concern is the common mode voltage from each stack to the ground, which requires an isolated DC-DC converter for each fuel cell to ensure insulation at the highest DC bus voltage level.

As shown in Figure 9.24, the CMI circuit arrangement can be extended to a three-phase modular multilevel converter (MMC), which consists of two complementary CMIs in a series stack for each phase, or leg. Each leg consists of two arms. Each arm is a single-phase CMI. The middle point between two arms is inserted with the inductors. Using phase-a as an example, the two inductors are denoted as L_{a1} and L_{a2}. This structure provides both high-voltage DC output, V_{dc}, and AC output, v_a, v_b, and v_c. The AC output can be directly connected to a high-voltage grid through the grid source inductors, L_s. This type of circuit configuration has also been extensively studied in battery energy storage systems for the state-of-charge control [143–146].

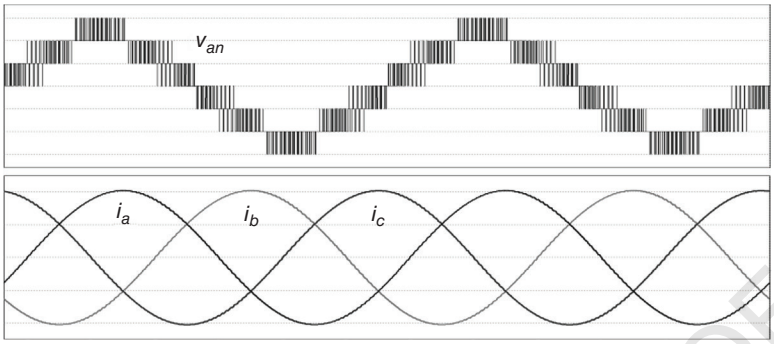

Figure 9.23 Output voltage and current waveforms of a cascaded multilevel inverter.

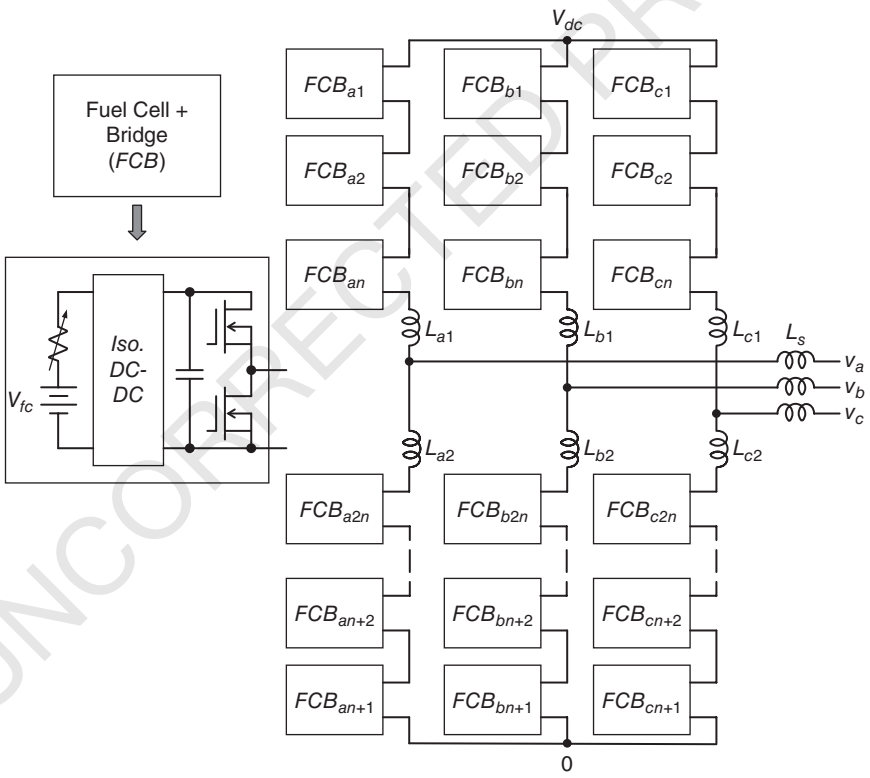

Figure 9.24 A large fuel cell system employing a three-phase modular multilevel converter.

9.6.3 Double-Line Frequency Issues

The voltage source inverter switching devices require anti-paralleled diodes to allow load current freewheeling. These freewheeling currents occur every time a switch is turned off. Looking from the DC input, the freewheeling current presents a high double-line-frequency content. All the single-phase and cascaded multilevel inverters have the double-line frequency ripple at the inverter input side, which can propagate back to the fuel cell. To understand the impact of the double-line frequency ripple to the fuel cell, the first attempt was to identify the transient behavior of the reactant concentrations within the stack, and of mass diffusion within the electrode under inverter loads with frequencies between 30 Hz and 1250 Hz [147]. In [148, 149] the study indicated that the fuel cell stack is not disturbed if its current frequency is higher than 10 kHz or lower than 1 Hz. However, at the double-line frequency of 100 Hz, the fuel cell voltage and current characteristic presents a hysteresis effect that can result in addition losses. References [150, 151] further verified that the double-line frequency can impact the fuel cell efficiency and maximum available power output.

Adding a large electrolytic capacitor or an ultracapacitor [58] can suppress the double-line frequency ripple, but the size, cost, and reliability are major concerns. Active ripple cancellation allows significant size reduction. Adding a paralleled branch to serve as the ripple port or active filter is possible to reduce the double-line frequency flowing back to fuel cells [152, 153]. For a system with two stages including a front-end DC-DC converter and a subsequent DC-AC inverter, the simplest solution is to design a high gain at the double-line frequency in the current loop controller for the existing DC-DC converter [154–160]. Of particular interest is a novel controller proposed in [160, 161], shown in Figure 9.25. This method employs a notch filter in the feedback loop for the DC bus voltage V_{dc}. The output of notch filter $V_{dc\text{-}n}$ serves as the feedback signal for the voltage loop control. The comparison of the DC bus reference voltage V_{dc}^{*} and $V_{dc\text{-}n}$ yields a signal which feeds into a voltage loop with proportional-integral (PI) controller $G_v(s)$. The output of $G_v(s)$ serves as the DC bus current reference I_{dc}^{*}, which compares with the current feedback I_{dc} to obtain an error signal that feeds into a PI plus proportional resonant (PR) controller $G_c(s)$ with resonant frequency equal to $2{\cdot}f_1$, and the output of $G_c(s)$ is fed into a PWM controller for DC-DC converter control. The inverter-side current loop controller $G_i(s)$ is also a PI+PR controller except that its resonant frequency is f_1.

Figure 9.26 compares the experimental voltage and current waveforms with a capacitor bank, and with the same capacitor bank but adding a PI+PR controller in the control loop. With the added PI+PR controller in the current loop, the fuel cell voltage and current ripples are significantly reduced. Physically, the double-line frequency ripple still exists on the inverter side, i_{inv}, but with a control loop that has sufficient gain at $2f_1$ such that the ripples are eliminated or significantly reduced at the DC side, or I_{dc}. In other words, the DC bus capacitor C_{dc} needs to absorb the ripple current. Nevertheless, the approach is very attractive and can effectively suppress the double-line frequency ripple without adding any components or extra cost.

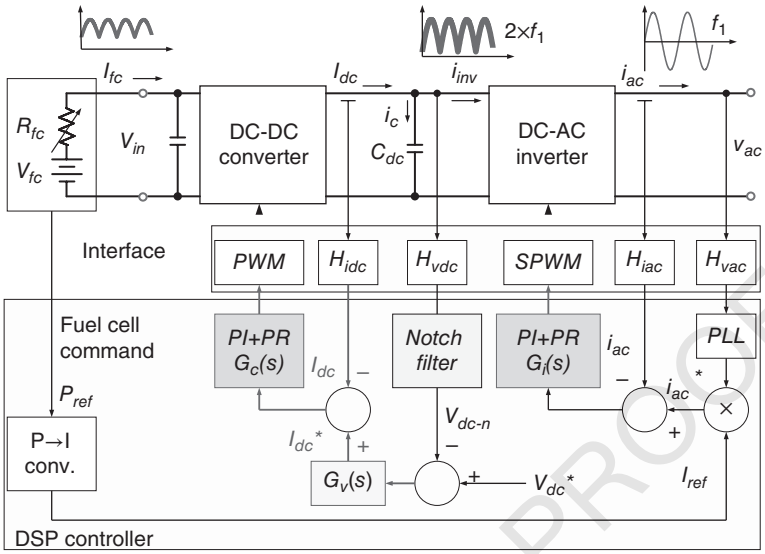

Figure 9.25 Block diagram of a two-stage single-phase inverter that implements a novel PI+PR controller for double-line frequency ripple reduction.

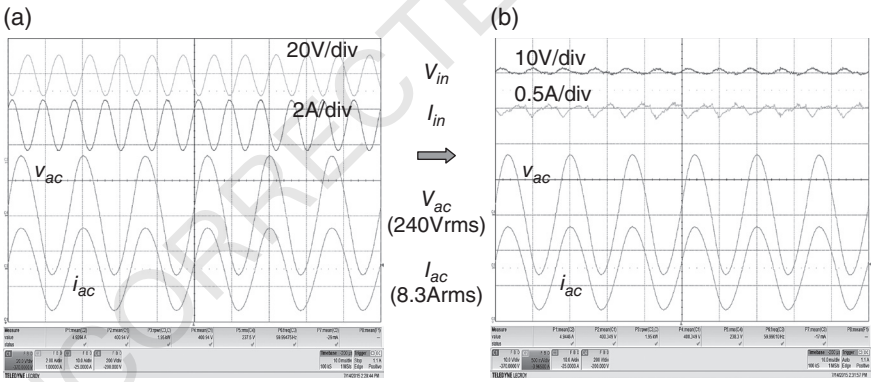

Figure 9.26 Experimental results of a current loop controller: (a) with a capacitor bank, and (b) with the same capacitor bank, but added PI+PR control in the control loop.

9.7 SUMMARY

Fuel cell systems exhibit attractive features that make them appealing in stationary power systems and transportation applications. Unlike other power sources such as PVs, the fuel cell system has a BOP to control the static and dynamic characteristics of the power output. As long as the fuel cell system is connected to a reliable source

of fuel such as hydrogen, natural gas, methanol, or ammonia, it can continuously provide power to the load, making it more desirable for distributed generation than PVs or wind. Furthermore, different fuel cell technologies can be chosen to align with specific application requirements. For example, low-temperature fuel cells exhibit low-cost, high power density, and rapid start-up, making them suitable for transportation applications as well as for stationary power, provided the stationary application can use low-grade heat. High-temperature fuel cells, on the other hand, are more compatible with natural gas operation and provide high temperature heat, thus making them more suitable for stationary applications, where they can operate in cogeneration with a system efficiency approaching 90%.

Although hydrogen has been the default fuel for fuel cells, simple hydrocarbons, simple alcohols, and even ammonia can be reformed to generate hydrogen or used directly as the fuel. The successful development of fuel cells that can directly use alternative fuels such as methanol and ammonia could significantly simplify the fuel distribution and storage infrastructure and expand the opportunities for fuel cell commercialization.

The low voltage provided by individual fuel cells necessitates stacking a high number of fuel cells to meet the voltage requirement for larger systems. For large stacks, the BOP required to keep individual cells supplied with reactants and maintained at appropriate temperature and moisture conditions can be challenging. For stationary power system applications, one of the major challenges for the power management system is to convert low-voltage DC to high-voltage AC while complying with the grounding requirement for the source. For transportation applications, however, grounding is not required by regulations, but the dynamic response is a major concern, and an energy management system incorporating external batteries with bi-directional chargers is necessary.

For high-power applications, the availability of semiconductor devices and components and the package-related parasitics can impact the power conversion performance, especially the efficiency. As outlined in this chapter, different design options for DC-DC and DC-AC power conversion circuits are available to accommodate different power levels and operating requirements. For a source supplying to a single-phase AC load, the double-line frequency ripple propagating from the inverter back to the fuel cell source may reduce the fuel cell life expectancy and the fuel efficiency. As reviewed in this chapter, a recently developed approach with a two-stage power conversion and advanced control techniques provides a solution for addressing this concern that is cost-effective. Experimental waveforms using this two-stage approach show that that it can significantly improve the performance without adding extra components.

REFERENCES

[1] J.-S. Lai and M. Ellis. "Fuel Cell Power Systems and Applications," *IEEE Proceedings*, vol. 105, no. 11, pp. 2166–2190, 2017.

[2] M. LaMonica. "GE Claims Fuel Cell Breakthrough, Starts Pilot Production," *IEEE Spectrum*, 1, July 25, 2014.
[3] S. Samuelsen. "Why the Automotive Future Will Be Dominated by Fuel Cells," *IEEE Spectrum*. 1, Dec. 6, 2016.
[4] J. O'dell. "Toyota's Heavy-Duty Fuel Cell Truck Finally Hits the Road," *Trucks*, 1, Oct. 12, 2017.
[5] K. A. Mauritz and R. B. Moore. "State of understanding of Nafion," *Chemical Reviews*, vol. 104, no. 10, pp. 4535–4585, Oct. 2004.
[6] H. W. Zhang and P. K. Shen. "Recent Development of Polymer Electrolyte Membranes for Fuel Cells," *Chemical Reviews*, vol. 112, no. 5, pp. 2780–2832, May 2012.
[7] H. A. Gasteiger, S. S. Kocha, B. Sompalli and F. T. Wagner. "Activity benchmarks and requirements for Pt, Pt-alloy, and non-Pt oxygen reduction catalysts for PEMFCs," *Applied Catalysis B-Environmental*, vol. 56, no. 1–2, pp. 9–35, Mar. 10 2005.
[8] *Multi-year Research Development and Demonstration Plan*. Available online at https://energy.gov/eere/fuelcells/downloads/fuel-cell-technologies-office-multi-year-research-development-and-22, 2016.
[9] E. Proietti et al. "Iron-based cathode catalyst with enhanced power density in polymer electrolyte membrane fuel cells," *Nature Communications*, vol. 2, p. 9, Aug. 2011, Art. no. 416.
[10] G. Wu, K. L. More, C. M. Johnston and P. Zelenay. "High-Performance Electrocatalysts for Oxygen Reduction Derived from Polyaniline, Iron, and Cobalt," *Science*, vol. 332, no. 6028, pp. 443–447, Apr. 2011.
[11] R. Borup et al. "Scientific aspects of polymer electrolyte fuel cell durability and degradation," *Chemical Reviews*, vol. 107, no. 10, pp. 3904–3951, Oct. 2007.
[12] S. Maass, F. Finsterwalder, G. Frank, R. Hartmann and C. Merten. "Carbon support oxidation in PEM fuel cell cathodes," *Journal of Power Sources*, vol. 176, no. 2, pp. 444–451, Feb. 1 2008.
[13] S. Sharma and B. G. Pollet. "Support materials for PEMFC and DMFC electrocatalysts – A review," *Journal of Power Sources*, vol. 208, pp. 96–119, June 2012.
[14] A. Kusoglu, A. M. Karlsson, M. H. Santare, S. Cleghorn and W. B. Johnson. "Mechanical response of fuel cell membranes subjected to a hygro-thermal cycle," *Journal of Power Sources*, vol. 161, no. 2, pp. 987–996, Oct. 2006.
[15] Y. Q. Li et al. "Experimental Measurement of Stress and Strain in Nafion Membrane during Hydration Cycles," *Journal of the Electrochemical Society*, vol. 159, no. 2, pp. B173–B184, 2012.
[16] I. S. Hussaini and C. Y. Wang. "Visualization and quantification of cathode channel flooding in PEM fuel cells," *Journal of Power Sources*, vol. 187, no. 2, pp. 444–451, Feb. 2009.
[17] H. Li *et al*. "A review of water flooding issues in the proton exchange membrane fuel cell," *Journal of Power Sources*, vol. 178, no. 1, pp. 103–117, Mar. 2008.
[18] Y. Wang, S. Basu and C. Y. Wang. "Modeling two-phase flow in PEM fuel cell channels," *Journal of Power Sources*, vol. 179, no. 2, pp. 603–617, May 2008.
[19] I. Fuel Cell Energy. *Fuel Cell Energy Home Page*. Available online at http://www.fuelcellenergy.com/, 2 March 2017.
[20] R. Remick and D. Wheeler. "Molten Carbonate and Phosphoric Acid Stationary Fuel Cells: Overview and Gap Analysis," National Renwable Energy Laboratory September, 2010. Available online at www1.eere.energy.gov/hydrogenandfuelcells/pdfs/49072.pdf
[21] K. Stanton and J.-S. Lai. "A thermally dependent fuel cell model for power electronics design," *Proc. IEEE Power Electron. Specialists Conf*., Recife, Brazil, 2005, pp. 1647–1651.
[22] J. R. Varcoe et al. "Anion-exchange membranes in electrochemical energy systems," *Energy & Environmental Science*, vol. 7, no. 10, pp. 3135–3191, Oct. 2014.
[23] E. Antolini and E. R. Gonzalez. "Alkaline direct alcohol fuel cells," *Journal of Power Sources*, vol. 195, no. 11, pp. 3431–3450, June 2010.
[24] M. M. Mench. *Fuel Cell Engines*. Hoboken, NJ: John Wiley & Sons, Inc., 2008.
[25] S. F. Lu, J. Pan, A. B. Huang, L. Zhuang and J. T. Lu. "Alkaline polymer electrolyte fuel cells completely free from noble metal catalysts," *Proceedings of the National Academy of Sciences of the United States of America*, vol. 105, no. 52, pp. 20611–20614, Dec. 2008.
[26] S. Gottesfeld et al. "Anion exchange membrane fuel cells: current status and remaining challenges," *Journal of Power Sources*, vol. 375, pp. 170–184, 2018.

[27] N. Sammes, R. Bove and K. Stahl. "Phosphoric acid fuel cells: Fundamentals and applications," *Current Opinion in Solid State & Materials Science*, vol. 8, no. 5, pp. 372–378, Oct. 2004.
[28] E. G. G. Technical Services. *Fuel Cell Handbook* (7th ed.), Morgantown, WV: National Energy Technology Laboratory, 2004.
[29] Q. F. Li, J. O. Jensen, R. F. Savinell and N. J. Bjerrum. "High temperature proton exchange membranes based on polybenzimidazoles for fuel cells," *Progress in Polymer Science*, vol. 34, no. 5, pp. 449–477, May 2009.
[30] C. Zamfirescu and I. Dincer. "Using ammonia as a sustainable fuel," *Journal of Power Electronics*, vol. 185, pp. 459–465, 2008.
[31] X. L. Li and A. Faghri. "Review and advances of direct methanol fuel cells (DMFCs) part I: Design, fabrication, and testing with high concentration methanol solutions," *Journal of Power Sources*, vol. 226, pp. 223–240, Mar. 2013.
[32] M. Ahmed and I. Dincer. "A review on methanol crossover in direct methanol fuel cells: challenges and achievements," *International Journal of Energy Research*, vol. 35, no. 14, pp. 1213–1228, Nov. 2011.
[33] H. Yang, T. S. Zhao, and Q. Ye. "In situ visualization study of CO_2 gas bubble behavior in DMFC anode flow fields," *Journal of Power Sources*, vol. 139, no. 1–2, pp. 79–90, Jan. 2005.
[34] Y. Yan and S. Gottesfeld. "Direct ammonia fuel cell utilizing an OH- ion conducting membrane electrolyte," NH3 Fuel Conference, Minneapolis 2017.
[35] A. Afif, N. Radenahmad, Q. Cheok, S. Shams and J. H. Kim. "Ammonia-fed fuel cells: a comprehensive review," *Renewable and Sustainable Energy Reviews*, vol. 60, pp. 822–835, 2016.
[36] W. Wang, J. M. Herreros, A. Tsolakis and A. York. "Ammonia as hydrogen carrier for transportation; investigation of the ammonia exhaust gas fuel reforming," *International Journal of Hydrogen Energy*, vol. 38, pp. 9907–9917, 2013.
[37] J. A. Kilner and M. Burriel. "Materials for Intermediate-Temperature Solid-Oxide Fuel Cells." In *Annual Review of Materials Research,* vol. 44, edited by D. R. Clarke, pp. 365–393, 2014.
[38] A. J. Appleby. "Fuel cell technology: Status and future prospects," *Energy, Review* vol. 21, no. 7–8, pp. 521–653, July–Aug. 1996.
[39] Atrex Energy. Available online at http://www.atrexenergy.com/
[40] T. A. Adams, J. Nease, D. Tucker and P. I. Barton. "Energy Conversion with Solid Oxide Fuel Cell Systems: A Review of Concepts and Outlooks for the Short- and Long-Term," *Industrial & Engineering Chemistry Research, Review* vol. 52, no. 9, pp. 3089–3111, Mar. 2013.
[41] A. J. Jacobson. "Materials for Solid Oxide Fuel Cells," *Chemistry of Materials*, vol. 22, no. 3, pp. 660–674, Feb. 2010.
[42] C. Haynes and W. J. Wepfer. "'Design for power' of a commercial grade tubular solid oxide fuel cell," *Energy Conversion and Management*, vol. 41, no. 11, pp. 1123–1139, July 2000.
[43] S. J. McPhail, L. Leto, M. D. Pietraand A. Moreno. "International Status of Molten Carbonate Fuel Cell Technology," ENEA, Italian National Agency for New Technologies, Energy and Sustainable Economic Development 2015. Available online at http://www.ieafuelcell.com/documents/MCFC_international_status_2015_web.pdf
[44] USCAR. *Who We Are*. Available online at www.uscar.org/guest/about/
[45] O. Groger, H. A. Gasteiger and J. P. Suchsland. "Review – Electromobility: Batteries or Fuel Cells?" *Journal of the Electrochemical Society, Review* vol. 162, no. 14, pp. A2605–A2622, 2015.
[46] F. T. Wagner, B. Lakshmanan and M. F. Mathias. "Electrochemistry and the Future of the Automobile," *Journal of Physical Chemistry Letters*, vol. 1, no. 14, pp. 2204–2219, July 2010.
[47] K. G. Gallagher et al. "Quantifying the promise of lithium-air batteries for electric vehicles," *Energy & Environmental Science*, vol. 7, no. 5, pp. 1555–1563, May 2014.
[48] Office of Energy Efficiency and Renewable Energy. *Compare Fuel Cell Vehicles*. Available online at https://www.fueleconomy.gov/feg/fcv_sbs.shtml
[49] *Progress Report for Hydrogen, Fuel Cells, and Infrastructure Technologies Program*. Available online at https://energy.gov/sites/prod/files/2014/03/f11/33098.pdf, 2002.

[50] M. Wang. "Fuel choices for fuel-cell vehicles: well-to-wheels energy and emission impacts," *Journal of Power Sources*, vol. 112, no. 1, pp. 307–321, Oct. 2002, Article no. Pii s0378-7753(02)00447-0.

[51] I. Staffell and R. Green. "The cost of domestic fuel cell micro-CHP systems," *International Journal of Hydrogen Energy*, vol. 38, no. 2, pp. 1088–1102, Jan. 2013.

[52] T. Elmer, M. Worall, S. Y. Wu and S. B. Riffat. "Fuel cell technology for domestic built environment applications: State of-the-art review," *Renewable & Sustainable Energy Reviews*, Review vol. 42, pp. 913–931, Feb. 2015.

[53] H. R. Ellamla, I. Staffell, P. Bujlo, B. G. Pollet and S. Pasupathi. "Current status of fuel cell based combined heat and power systems for residential sector," *Journal of Power Sources*, Review vol. 293, pp. 312–328, Oct. 2015.

[54] C. S. Wang, M. H. Nehrir and S. R. Shaw. "Dynamic models and model validation for PEM fuel cells using electrical circuits," *IEEE Transactions on Energy Conversion*, vol. 20, no. 2, pp. 442–451, June 2005.

[55] J. M. Correa, F. A. Farret, L. N. Canha and M. G. Simoes. "An electrochemical-based fuel-cell model suitable for electrical engineering automation approach," *IEEE Transactions on Industrial Electronics*, vol. 51, no. 5, pp. 1103–1112, Oct. 2004.

[56] M. Uzunoglu and M. S. Alam. "Dynamic modeling, design, and simulation of a combined PEM fuel cell and ultracapacitor system for stand-alone residential applications," *IEEE Transactions on Energy Conversion*, vol. 21, no. 3, pp. 767–775, Sept. 2006.

[57] L. Y. Chiu, B. Diong and R. S. Gemmen. "An Improved Small-Signal Model of the Dynamic Behavior of PEM Fuel Cells" *IEEE Trans. Ind. Appl.*, vol. 40, no. 4, pp. 970–977, 2004.

[58] M. Schenck, J.-S. Lai and K. Stanton. "Fuel Cell and Power Conditioning System Interactions," *Proc. IEEE Appl. Power Electron. Conf*., Austin, TX, 2005, pp. 114–120.

[59] W. A. Fuglevand, P. D. DeVries, G. A. Lloyd, D. R. Lott and J. P. Scartozzi. "Fuel Cell and Method for Controlling Same," US Patent No. 6096449, 2000.

[60] W. A. Fuglevand and J. Dodge. "Fuel Cell Power Systems, Direct Current Voltage Converters, Fuel Cell Power Generation Methods, Power Conditioning Methods and Direct Current Conditioning Methods," USA Patent No. 6428918, Aug. 6, 2002.

[61] T. Nergaard, J. Ferrell, L. Leslie and J.-S. Lai. "Design Considerations for a 48 V Fuel Cell to Split Single Phase Inverter System with Ultracapacitor Energy Storage," *Proc. IEEE Power Electron. Specialists Conf*., Cairns, Australia, 2002, pp. 2007–2012.

[62] C. Liu, A. Johnson and J.-S. Lai. "A novel three-phase high-power soft-switched DC/DC converter for low-voltage fuel cell applications," *IEEE Trans. Ind. Appl.*, vol. 41, no. 6, pp. 1691–1697, 2005.

[63] C. Liu, A. Ridenour and J.-S. Lai. "Modeling and control of a novel six-leg three-phase high-power converter for low voltage fuel cell applications," *IEEE Trans. Power Electron.*, vol. 21, no. 5, pp. 1292–1300, 2006.

[64] J.-S. Lai and D. J. Nelson. "Energy management power converters in hybrid electric and fuel cell vehicles," *IEEE Proc.*, vol. 95, no. 4, pp. 766–777, 2007.

[65] K. Rajashekara. "Power Conversion and Control Strategies for Fuel Cell Vehicles," *Proc. IEEE Ind. Electron. Conf*., Roanoke, VA, 2003, pp. 2865–2870.

[66] L. Palma and P. N. Enjeti. "A Modular Fuel Cell, Modular DC–DC Converter Concept for High Performance and Enhanced Reliability," *IEEE Trans. Power Electron.*, vol. 24, no. 6, pp. 1437–1443, June 2009.

[67] J. T. Hawke, H. S. Krishnamoorthy and P. N. Enjeti. "A New Utility-Scale Power Converter for Large Fuel Cell Power Plants with Individual Stack Power Control," *Proc. IEEE Appl. Power Electron. Conf*., Orlando, FL, 2012, pp. 1482–1488.

[68] J. T. Hawke, H. S. Krishnamoorthy and P. N. Enjeti. "A Family of New Multiport Power-Sharing Converter Topologies for Large Grid-Connected Fuel Cells," *IEEE Journal of Emerging and Selected Topics in Power Electron.*, vol. 2, no. 4, pp. 962–971, Dec. 2014.

[69] J. Wang. "Practical Design Considerations of Power Electronics in Hybrid and Fuel Cell Vehicles" *Proc. IEEE Vehicle Power and Propulsion Conf*., Harbin, China, 2008, pp. 1–6.

[70] A. Emadi, S. S. Williamson and A. Khaligh. "Power Electronics Intensive Solutions for Advanced Electric, Hybrid Electric, and Fuel Cell Vehicular Power Systems," *IEEE Trans. Power Electron.*, vol. 21, no. 3, pp. 567–577, May 2006.
[71] U. R. Prasanna, A. K. Rathore and S. K. Mazumder. "Novel Zero-Current-Switching Current-Fed Half-Bridge Isolated DC/DC Converter for Fuel-Cell-Based Applications," *IEEE Trans. Ind. Appl.,* vol. 49, no. 4, pp. 1658–1668, Jul./Aug. 2013.
[72] U. R. Prasanna, X. Pan, A. K. Rathore and K. Rajashekara. "Propulsion System Architecture and Power Conditioning Topologies for Fuel Cell Vehicles," *IEEE Trans. Ind. Appl.*, vol. 51, no. 1, pp. 640–650, 2015.
[73] K. Wang, C.-Y. Lin, L. Zhu, D. Qu, F. C. Lee and J.-S. Lai. "Bi-directional DC to DC converters for fuel cell systems," *Proc. IEEE Power Electron. in Transportation*, 1998, pp. 47–51.
[74] C. Liu et al. "Power balance control and voltage conditioning for fuel cell converter with multiple sources," *Proc. IEEE Power Electron. Specialists Conf*., Cairns, Australia, 2002, vol. 4, pp. 2001–2006.
[75] NFPA. *National Electric Code*, 2014 ed. (NFPA 70), Quincy, MA: NFPA, 2013, p. 920.
[76] P. Krein. *Elements of Power Electronics*, Oxford: Oxford University Press, 2014, p. 816.
[77] N. Mohan. *Power Electronics – A First Course*. Hoboken, NJ: John Wiley & Sons, 2012, p. 286.
[78] R. W. Erickson and D. Maksimovic. *Fundamentals of Power Electronics*, Berlin: Springer, 2001.
[79] Q. Zhao and F. C. Lee. "High-efficiency, high step-up dc–dc converters," *IEEE Trans. Power Electron.*, vol. 18, no. 1, pp. 65–73, 2003.
[80] B. Gu, J. Dominic, J.-S. Lai, Z. Zhao and C. Liu. "High boost ratio hybrid transformer DC–DC converter for photovoltaic module applications," *IEEE Transactions on Power Electronics*, vol. 28, no. 4, pp. 2048–2058, 2013.
[81] B. Gu, J. Dominic, J.-S. Lai and H. Ma. "Hybrid transformer ZVS/ZCS DC-DC converter for photovoltaic microinverters," *IEEE Applied Power Electronics Conference and Exposition (APEC)*, 2013, pp. 16–22.
[82] B. Gu, J. Dominic, B. Chen, L. Zhang and J.-S. Lai. "Hybrid transformer ZVS/ZCS DC–DC converter with optimized magnetics and improved power devices utilization for photovoltaic module applications," *IEEE Transactions on Power Electronics*, vol. 30, no. 4, pp. 2127–2136, 2015.
[83] S. K. Changchien, T. J. Liang, J. F. Chen and L. S. Yang. "Novel high step-up DC–DC converter for fuel cell energy conversion system," *IEEE Trans. Ind. Electron.*, vol. 57, no. 6, pp. 2007–2017, 2010.
[84] R. J. Wai and R. Y. Duan. "High step-up converter with coupled-inductor," *IEEE Trans. Power Electron.*, vol. 20, no. 5, pp. 1025–1035, 2005.
[85] Y. P. Hsieh, J.-F. Chen, T. J. Liang and L. S. Yang. "A novel high step-up DC–DC converter for a microgrid system," *IEEE Trans. Power Electron.*, vol. 26, no. 4, pp. 1127–1136, 2011.
[86] W. Yu et al. "High efficiency converter with charge pump and coupled inductor for wide input photovoltaic AC module applications," *IEEE Energy Conversion Congress and Exposition*, 2009, pp. 3895–3900.
[87] W. H. Li and X. N. He. "Review of non-isolated high step-up DC/DC converters in photovoltaic grid-connected applications," *IEEE Trans. Ind. Elect*, vol. 58, no. 4, pp. 1239–1250, 2011.
[88] E. H. Ismail, M. A. Saffar, A. J. Sabzali and A. A. Fardoun. "A family of single-switch PWM converters with high step-up conversion ratio," *IEEE Trans. Circuits System.*, vol. 55, no. 4, pp. 1159–1171, 2008.
[89] W. Yu, B. York and J.-S. Lai. "Inductorless forward-flyback soft-switching converter with dual constant on-time modulation for photovoltaic applications," *Proc. IEEE Energy Conv. Congress and Expo*., 2012, pp. 3549–3555.
[90] L. Huber and M. Jovanovic. "Forward-Flyback Converter with Current-Doubler Rectifier: Analysis, Design, and Evaluation Results," *IEEE Trans. Power Electron.*, vol. 14, no. 1, pp. 184–192, 1999.
[91] L. Chen, H. Hu, Q. Zhang, A. Amirahmadi and I. Batarseh. "A Boundary-Mode Forward-Flyback Converter With an Efficient Active LC Snubber Circuit," *IEEE Trans. Power Electron.*, vol. 29, no. 6, pp. 2044–2058, 2014.

[92] K.-C. Tseng, J.-Z. Chen, J.-T. Lin, C.-C. Huang and T.-H. Yen. "High Step-Up Interleaved Forward-Flyback Boost Converter With Three-Winding Coupled Inductors," *IEEE Trans. Power Electron.*, vol. 30, no. 9, pp. 4696–4703, 2015.

[93] J. Lee, J. Park and H. Jeon. "Series-connected forward-flyback converter for high step-up power conversion," *IEEE Trans. Power Electron.*, vol. 26, no. 12, pp. 3629–3641, Dec. 2011.

[94] T.-H. Hsia, H.-Y. Tsai, D. Chen, M. Lee and C.-S. Huang. "Interleaved Active-Clamping Converter With ZVS/ZCS Features," *IEEE Trans. Power Electron.*, vol. 26, no. 1, pp. 29–37, Jan. 2011.

[95] K. Wang, F. C. Lee and J.-S. Lai. "Operation Principles of Bi-directional Full-Bridge DC/DC Converter with Unified Soft-Switching Scheme and Soft-Starting Capability," *Proc. IEEE Appl. Power Electron. Conf.*, New Orleans, LA, 2000, pp. 111–118.

[96] K. Wang, J.-S. Lai and F. C. Lee. "Design, Implementation, and Experimental Results of Bi-directional Full-bridge DC/DC Converter with Unified Soft-switching Scheme and Soft-starting Capability," *Proc. IEEE Power Electron. Specialists Conf.*, Galway, Ireland, 2000, pp. 1058–1063.

[97] L. H. Mweene, C. A. Wright and M. F. Schlecht. "A 1 kW 500 kHz front-end converter for a distributed power supply system," *IEEE Trans. Power Electron.*, vol. 6, no. 3, pp. 398–407, July 1991.

[98] J. A. Sabate, V. Vlatkovic, R. B. Ridley, F. C. Lee and B. H. Cho. "Design considerations for high-voltage high-power full-bridge zero-voltage-switched PWM converter," *Proc. IEEE Appl. Power Electron. Conf.*, Los Angeles, CA, 1990, pp. 275–284.

[99] W. S. Yu, J.-S. Lai and H. Qian. "A Family of Novel Zero-Voltage and Zero-Current Switching Full Bridge Converters Using Output Voltage Reset for Fuel Cell Application," *Con. Record IEEE IAS Annual Meeting*, Pittsburgh, 2007, pp. 622–627.

[100] B. Gu, J.-S. Lai, N. Kees and C. Zheng. "Hybrid-switching full-bridge DC–DC converter with minimal voltage stress of bridge rectifier, reduced circulating losses, and filter requirement for electric vehicle battery chargers," *IEEE Trans. Power Electron.*, vol. 28, no. 3, pp. 1132–1144, 2013.

[101] S. Cuk. "Voltage Step-up Switching DC-DC Converter," Patent No. 7778046, 2010.

[102] S. Cuk. "Step-Down Converter Having a Resonannt Inductor, a Resonant Caapacitor and a Hybrid Transformer," Patent No. 7915874, 2011.

[103] S. Cuk. "Hybrid-Switching Step-Down Converter with a Hybrid Transformer," Patent No. 9231471, 2016.

[104] C. Adragna, S. De Simone and C. Spini. "Designing LLC resonant converters for optimum efficiency," *Proc. Eur. Conf. Power Electron. Appl.*, 2009, pp. 1–10.

[105] R. Beirangand, B. Rashidian, M. R. Zolghadri and S. M. H. Alvai. "Using LLC resonant converter for designing wide-range voltage source," *IEEE Trans. Ind. Electron.*, vol. 58, no. 5, pp. 1746–1756, May 2011.

[106] B. Lu, W. Liu, Y. Liang, F. C. Lee and J. D. van Wyk. "Optimal design methodology for LLC resonant converter," *Proc. IEEE Appl. Power Electron. Conf.*, Dallas, TX, 2006, pp. 19–23.

[107] F. Canales, P. Barbosa and F. C. Lee. "A wide input voltage and load output variations fixed-frequency ZVS DC/DC LLC resonant converter for high-power application," *Proc. IEEE Appl. Power Electron. Conf.*, Dallas, TX, 2002, pp. 2306–2313.

[108] M. Jovanovic and B. T. Irving. "On-the-Fly Topology-Morphing Control–Efficiency Optimization Method for LLC Resonant Converters Operating in Wide Input- and/or Output-Voltage Range," *IEEE Trans. Power Electron.*, vol. 31, no. 3, pp. 2596–2608, Mar. 2016.

[109] J.-S. Lai. "A high-performance V6 converter for fuel cell power conditioning system," *Proc. IEEE Conf. Vehicle Power and Propulsion*, Chicago, IL, 2005, pp. 624–630.

[110] C. Liu, A. Ridenour and J. S. Lai. "Modeling and Control of a Novel Six-Leg Three-Phase High-Power Converter for Low-Voltage Fuel Cell Applications," *IEEE Trans. Power Electron.*, vol. 21, no. 5, pp. 1292–1300, 2006.

[111] J.-S. Lai, S.-R. Moon, R. Kim, F.-Y. Lin, Y.-H. Liu and M.-H. Lin. "A general-purpose three-phase dc-dc converter building block for fuel cell applications," *Proc. IEEE Ind. Electron. Conf.*, 2007, pp. 1639–1644.

[112] S.-R. Moon and J.-S. Lai. "Multiphase Isolated DC-DC Converter for Low-Voltage High-Power Fuel Cell Applications," *Proc. IEEE Appl. Power Electron. Conf.*, Anaheim, CA, 2007, pp. 654–660.

[113] W. Lu, X. Wu, Z. Lu and Z. Qian. "Wide Input Voltage Isolated Dc-Dc Converter with Interleaving Control," *Proc. EPE-PEMC*, Portoroz, Slovenia, 2006, pp. 94–99.
[114] B. K. Bose. *Modern Power Electronics and AC Motor Drives*, Upper Saddle River, NJ: Prentice Hall, 2002.
[115] B. K. Bose. *Power Electronics and Motor Drives – Advances and Trends*, Burlington, MA: Elsevier, 2006.
[116] D. G. Holmes and T. A. Lipo. *Power Width Modulation for Power Converters*, Piscataway, NJ: IEEE Press, Wiley Interscience, 2003.
[117] J. A. Ferreira, P. C. Theron and J. D. van Wyk. "Component Loss Modeling in Hard Switched and Resonant Pole Inverters," *Conf. Rec. IEEE IAS Annual Meeting*, Detroit, MI, 1991, pp. 1462–1468.
[118] R. W. DeDoncker and J. P. Lyons. "The auxiliary quasi-resonant dc link inverter," *Proc. IEEE Power Electron. Specialists Conf*., 1991, pp. 248–253.
[119] B. Acharya and D. M. Divan. "Active Power Filters Using Resonant Pole Inverters," *IEEE Trans. Ind. Appl.,* vol. 28, no. 6, Nov. 1992.
[120] W. McMurray. "Resonant Snubbers with Auxiliary Switches," *IEEE Trans. Ind. Appl.*, vol. 29, no. 2, pp. 355–362, Mar. 1993.
[121] A. Toba, T. Shimizu and G. Kimura. "Auxiliary resonant commutated pole inverter using two internal voltage-points of DC source," *IEEE Trans. Ind. Electron.*, vol. 45, no. 2, pp. 200–206, Apr. 1998.
[122] J.-S. Lai, R. W. Young, G. W. Ott, J. W. McKeever and F. Z. Peng. "A delta-configured auxiliary resonant snubber inverter," *IEEE Trans. Ind. Appl.*, vol. 32, no. 3, pp. 518–525, 1996.
[123] J.-S. Lai et al. "Resonant snubber inverter," US Patent No. 5,642,273, 1997.
[124] J.-S. Lai. "Fundamentals of a new family of auxiliary resonant snubber inverters," *Proc. IEEE Ind. Electron. Conf*., New Orleans, LA, 1997, pp. 645–650.
[125] J.-S. Lai, J. Zhang, H. Yu and H. Kouns. "Source and load adaptive design for a high-power soft-switching inverter," *IEEE Trans. Power Electron.*, vol. 21, no. 6, pp. 1667–1675, 2006.
[126] W. Yu, J.-S. Lai and S.-Y. Park. "An improved zero-voltage switching inverter using two coupled magnetics in one resonant pole," *IEEE Trans. Power Electron.*, vol. 25, no. 4, pp. 952–961, 2010.
[127] J.-S. Lai et al. "A hybrid-switch-based soft-switching inverter for ultrahigh-efficiency traction motor drives," *IEEE Trans. Ind. Appl.*, vol. 50, no. 3, pp. 1966–1973, 2014.
[128] J.-S. Lai and W. Yu. "Hybrid switch for resonant power converters," US Patent No. 8,830,711, 2014.
[129] E. Faraci and J.-S. Lai. "Sensorless adaptive control of resonant snubber inverter for photovoltaic applications," *Proc. IEEE Ind. Electron. Conf*., Dallas, TX, 2014, pp. 1772–1778.
[130] B. Chen et al. "Design and optimization of 99% CEC efficiency soft-switching photovoltaic inverter," *Proc. IEEE Appl. Power Electron. Conf*., Long Beach, CA, 2013, pp. 946–951.
[131] C. Zheng et al. "An optimization design for 5-kW centralized PV inverter to achieve 99% efficiency," *Proc. IEEE Appl. Power Electron. Conf*., Long Beach, CA, 2013, pp. 2967–2970.
[132] R. Born, L. Zhang, Y. We, Q. Ma and J.-S. Lai. "Interleaved auxiliary resonant snubber for high-power, high-density applications," *Proc. IEEE Energy Conv. Congress and Expo*., 2016, pp. 1–6.
[133] B. Kou, H. Zhang, Y. Jin and H. Zhang. "An Improved Control Scheme for Single-Phase Auxiliary Resonant Snubber Inverter," *Proc. Int. Power Electron. and Motion Control Conf*., Hefei, China, 2016, pp. 1–5.
[134] H. Zhang, B. Kou, Y. Jin and H. Zhang. "Analysis of MOSFETs Switching Performance in Auxiliary Resonant Snubber Inverter," *Proc. IEEE Int. Power Electron. and Motion Control Conf*., Hefei, China, 2016, pp. 1–6.
[135] R. H. Baker and L. H. Bannister. "Electric power converter," USA Patent No. 3867643, 1975.
[136] R. H. Baker. "Switching Circuit," USA Patent No. 4210826, 1980.
[137] R. H. Baker. "Bridge Converter Circuit," USA Patent No. 4270163, 1981.
[138] J.-S. Lai, J. Stovall and F. Peng. "Multilevel converters for power system applications," *Proc. CIGRE SC 14 Int. Colloquium*, Montreal, Canada, 1995, pp. 7.3.1–7.3.7.

[139] J.-S. Lai and F. Z. Peng. "Multilevel converters – a new breed of power converters," *IEEE Trans. Ind. Appl.*, vol. 32, no. 3, pp. 509–517, 1996.
[140] J. Rodriguez, J.-S. Lai and F. Z. Peng. "Multilevel inverters: a survey of topologies, controls, and applications," *IEEE Trans. Ind. Electron.*, vol. 49, no. 4, pp. 724–738, 2002.
[141] B. Xiao, K. Shen, J. Mei, F. Filho and L. M. Tolbert. "Control of Cascaded H-Bridge Multilevel Inverter with Individual MPPT for Grid-Connected Photovoltaic Generators," *Proc. IEEE Energy Conv. Congress and Expo*., Raleigh, NC, 2012, pp. 3715–3711.
[142] B. Xiao, L. Hang, M. J. C. Riley, L. M. Tolbert and B. Ozpineci. "Modular Cascaded H-Bridge Multilevel PV Inverter With Distributed MPPT for Grid-Connected Applications," *IEEE Trans. Ind. Appl.,* vol. 51, no. 2, pp. 1722–1731, Mar./Apr. 2015.
[143] M. Hagiwara and H. Akagi. "Experiment and Simulation of a Modular Push–Pull PWM Converter for a Battery Energy Storage System," *IEEE Trans. Ind. Appl.*, vol. 50, no. 2, pp. 1131–1140, 2014.
[144] M. Xu, M. Tsirinomeny and A. Rufer. "A flexible and robust power management mechanism based on single-phase Modular Multilevel Converter with integrated energy storage elements," presented at the Proc. IEEE Ind. Electron. Conf., Yokohama, Japan, 2015.
[145] Q. Zhang, F. Gao and N. Li. "Multiple Time Scale Optimal Operation of MMC Battery Energy Storage System," *Proc. IEEE Energy Conv. Congress and Expo*., Montreal, Canada, 2015, pp. 1–7.
[146] B. Ren, Y. Xu and Q. Lan. "A Control Method for Battery Energy Storage System Based on MMC," presented at the IEEE Int. Future Energy Electron. Conf., Taipei, Taiwan, 2015.
[147] R. S. Gemmen. "Analysis for the effect of inverter ripple current on fuel cell operating condition," *ASME Trans.*, vol. 125, pp. 576–585, May 2003.
[148] G. Fontes, C. Turpin, S. Astier and T. A. Meynard. "Interactions Between Fuel Cells and Power Converters: Influence of Current Harmonics on a Fuel Cell Stack," *IEEE Trans. Power Electron.,* vol. 22, no. 2, p. 9, March 2007.
[149] G. Fontes, C. Turpin, R. Saisset, T. A. Meynard and S. Astier. "Interactions between fuel cells and power converters influence of current harmonics on a fuel cell stack," *Proc. IEEE Power Electron. Specialists Conf*., Aachen, Germany, 2004, pp. 4729–4735.
[150] S. K. Mazumder et al. "Solid-Oxide-Fuel-Cell Performance and Durability: Resolution of the Effects of Power-Conditioning Systems and Application Loads," *IEEE Trans. Power Electron.*, vol. 19, no. 5, pp. 1263–1278, Sept. 2004.
[151] W. Choi, P. N. Enjeti and J. W. Howze. "Development of an Equivalent Circuit Model of a Fuel Cell to Evaluate the Effects of Inverter Ripple Current," presented at the IEEE Applied Power Electron. Conf., Anaheim, CA, Feb. 2004.
[152] L. Cao, K. H. Loo and Y. M. Lai. "Frequency-Adaptive Filtering of Low-Frequency Harmonic Current in Fuel Cell Power Conditioning Systems," *IEEE Trans. Power Electron.*, vol. 30, no. 4, pp. 1966–1978, April 2015.
[153] P. Krein, R. S. Balog and M. Mirjafari. "Minimum Energy and Capacitance Requirements for Single-Phase Inverters and Rectifiers Using a Ripple Port," *IEEE Trans. Power Electron.*, vol. 27, no. 11, pp. 4690–4698, Nov. 2012.
[154] S. Moon, J. Lai, S. Park and C. Liu. "Impact of SOFC fuel cell source impedance on low frequency AC ripple," *Proc. IEEE Power Electron. Specialists Conf*., 2006, pp. 2037–2042.
[155] C. Liu and J. S. Lai. "Low Frequency Current Ripple Reduction Technique with Active Control in a Fuel Cell Power System with Inverter Load," *IEEE Trans. Power Electron.*, vol. 22, no. 4, pp. 1429–1436, 2007.
[156] J.-M. Kwon, E.-H. Kim, B.-H. Kwon and K.-H. Nam. "High-Efficiency Fuel Cell Power Conditioning System With Input Current Ripple Reduction," *IEEE Trans. Ind. Electron.*, vol. 56, no. 3, pp. 826–834, 2009.
[157] Z. Wei, X. Deng, C. Gong, J. Cheng, and F. Zhang. "A Novel Technique of Low Frequency Input Current Ripple Reduction In Two-stage DC-AC Inverter," *Proc. IEEE Ind. Electron. Conf*., Montreal, Canada, 2012, pp. 139–143.

[158] B. Gu, J. Dominic and J.-S. Lai. "Modeling and control of a high boost ratio PV module DC-DC converter with double grid-line ripple rejection," *Prof. IEEE Control and Modeling for Power Electron*., Salt Lake City, UT, 2013, pp. 1–4.

[159] X. Liu, H. Li and Z. Wang. "A Fuel Cell Power Conditioning System With Low-Frequency Ripple-Free Input Current Using a Control-Oriented Power Pulsation Decoupling Strategy," *IEEE Trans. Power Electron.*, vol. 29, no. 1, pp. 159–169, Jan. 2014.

[160] X. Zhao, L. Zhang, R. Born and J.-S. Lai. "Solution of input double-line frequency ripple rejection for high-efficiency high-power density string inverter in photovoltaic application," *Prof. IEEE Appl. Power Electron. Conf*., Long Beach, CA, 2016, pp. 1148–1154.

[161] B. Gu, J. Dominic, J. Zhang, L. Zhang, B. Chen and J.-S. Lai. "Control of electrolyte-free micro-inverter with improved MPPT performance and grid current quality," *Proc. IEEE Appl. Power Electron. Conf*., Fort Worth, TX, 2014, pp. 1788–1792.